Nanoscale

PAPER

Published on 25 November 2025
Licence and permissions

Cite this: *Nanoscale*, 2026, **18**, 843

Size-controlled CuO nanoparticles in KIT-6: magneto-photocatalytic properties and mechanistic insights

Sagnik Mitra,[a,b] Adarsh Kumar,[a,b] Deepak Tyagi,[a,b] Anindita Sarkar,[d] Sai Haranath Rekapalli,[e] Mayuresh D. Mukadam,[b,c] Ahin Roy,[d] Debasis Sen,[b,c] Kaustava Bhattacharyya *[a,b] and Avesh Kumar Tyagi *[b]

Size-dependent alterations in material properties, particularly changes in photocatalytic and magnetic behavior, have consistently attracted significant scientific interest. CuO nanoparticles were dispersed in mesoporous KIT-6 using the wet impregnation technique and the differences in the amount of CuO loadings led to alteration in the particle size with very narrow distribution. These materials were characterized using different techniques such as Small-Angle X-ray Scattering (SAXS), X-Ray Diffraction (XRD), X-ray Photoelectron Spectroscopy (XPS), High-Resolution Transmission Electron Microscopy (HR-TEM), Scanning Transmission Electron Microscopy (STEM), EELS mapping, EPR, *etc*. The SAXS study confirmed the presence of a three-dimensional cylindrical pore system in the synthesized KIT-6. These pores were filled without affecting the pore size or pore ordering with increasing CuO dispersion present as clusters within the channels of the mesoporous material. The magnetic properties along with the photocatalytic properties of CuO-KIT-6 (CK) were understood as a function of the particle size. The photocatalytic studies for the degradation of *ortho*-dichlorobenzene (*o*-DCB) showed these CKs to be good photocatalysts showing partial *o*-DCB degradation. The mechanism for the degradation of the *o*-DCB solution as a function of particle size is postulated in light of variation of magneto-photocatalytic properties.

Received 1st August 2025,
Accepted 17th November 2025

DOI: 10.1039/d5nr03258j

rsc.li/nanoscale

1. Introduction

All fundamental material properties, such as chemical, optical, mechanical, electrical, and magnetic, are mostly size-dependent.[1] Variation of properties at the nanometer regime is not just a result of scaling factors. In semiconductors, it results from the confinement of the electronic motion to a length scale that is comparable to or smaller than the length scale characterizing the electronic motion in a bulk semiconducting material. In the nano or subnano regime, the surface structure and electronic properties change dramatically, thereby altering their catalytic performance.[2–4] Cupric oxide (CuO) is a p-type semiconducting material[5,6] having a direct band gap. The direct band transition in bulk CuO is reported to be around 3.25 eV.[7] The fundamental band gap of CuO consists of localized states.[8–10] It therefore exhibits boundless potential for extensive applications as photoelectron materials,[11] gas sensors,[12] lithium-ion electrode materials,[13] field emission emitters,[14] and heterogeneous catalysts.[15] CuO crystallizes in a monoclinic structure with the space group $C2/c$, containing four formula units per unit cell. Each Cu^{2+} ion is coordinated by four O^{2-} ions, forming a distorted square planar geometry. This coordination environment gives rise to a complex magnetic structure associated with the Cu spin. The ground state of CuO is antiferromagnetic in nature;[16] however, unlike other antiferromagnetic semiconductor oxides that reside in a pure disordered paramagnetic state above the Néel temperature, CuO behaves as a 1D anti-ferromagnet.[17,18] There is alteration in the magnetic properties of CuO as a function of particle size and the alteration in the electronic properties affects both the magnetic and catalytic properties together[19–21] and CuO is no exception.

One of the ways to synthesize CuO nanoparticles of different sizes and shapes is the confinement of different amounts of CuO nanoparticles within the channels of a mesoporous matrix and modulating its magnetic and catalytic pro-

[a]*Chemistry Division, Bhabha Atomic Research Centre, Mumbai 400 085, India. E-mail: kaustava@barc.gov.in*
[b]*Homi Bhabha National Institute, Mumbai 400 094, India. E-mail: aktyagi@barc.gov.in*
[c]*Solid State Physics Division, Bhabha Atomic Research Centre, Mumbai 400 085, India*
[d]*Materials Science Centre, Indian Institute of Technology Kharagpur, West Bengal 721302, India*
[e]*Tata Institute of Fundamental Research, Homi Bhabha Road, Colaba, Mumbai 400005, India*

perties. A suitable choice will be the silica mesoporous matrix; it is diamagnetic in nature and possesses the required surface –OH groups which suitably augment the photocatalytic properties. Previously, the particle size of CuO was varied by adjusting the amount of copper loading on the SBA-15 support, altering its properties significantly.[22] Mesoporous materials that are silica-based in origin, such as MCM-*n*, SBA-*n*, FDU-*n*, KIT-*n*, *etc*. (*n* represents different mesoporous silica structures such as MCM-41, MCM-48, *etc*.), are synthesized using soft templates[23–25] and are commonly chosen for their high hydrothermal stability, attaining a large surface area (SA), variation in pore size, and a tunable structure.[26,27] Pal *et al.* used CuO anisotropic nanoparticles, supported on mesoporous SBA-15, for selective hydrogenation of nitro-aromatics mainly due to alteration in the surface area.[28] Rahmani *et al.* reported enhanced degradation of the antibiotic tetracycline using MCM-41-supported titania decorated with CuO nanoparticles, which was attributed to the formation of less agglomerates when dispersed over the support material.[29] Wu *et al.* reported the photocatalytic degradation of methylene orange using nanocomposites of ZnO–CuO dispersed over SBA-15, and the adsorption ability and loading percentage of these nanocomposites were determined as the major factors causing the photocatalytic degradation.[30] Among these materials, KIT-6 exhibits a three-dimensional cubic structure with *Ia*3*d* symmetry, characterized by interpenetrating cylindrical pores and interconnected mesoporous channels. Owing to its highly ordered 3D architecture and extensive pore connectivity, KIT-6 is particularly well suited for applications in photocatalysis, facilitating efficient mass transport and active site accessibility.

Polychlorodibenzodioxins (PCDDs) and polychlorodibenzofurans (PCDFs) belonging to the Dioxins and Furans (D&Fs) family are A1 carcinogens, and owing to their high toxicity, high biological half-life, high environmental persistence, bioaccumulation, and carcinogenicity, they should not be present in the atmosphere; they need to be either completely degraded, usually thermally, or mineralized to CO_2.[31,32] As PCDDs and PCDFs are highly toxic and costly, they are usually represented by *ortho*-dichlorobenzene (*o*-DCB), which has a structure similar to 2,3,7,8-tetrachlorodibenzodioxin (TCDD), and their chemical interaction and sorption parameters are also almost similar. Photocatalysis offers certain advantages such as operation under ambient conditions, utilization of renewable solar energy, and the potential for complete mineralization of pollutants.[33] Complete photocatalytic degradation of *o*-DCB in the solution phase has a virtuous challenging prospect as the common degradation pathway of D&Fs affecting human beings and animals through the food chain. However, D&Fs and *o*-DCB are sparingly soluble in water and are more soluble in fats and lipids. Photocatalysis has emerged as a highly promising technology for the efficient degradation of such pollutants into less harmful by-products.[34,35]

The degradation of *o*-DCB by bulk CuO on its own is not particularly the most effective in the liquid phase mostly due to its tendency to aggregate in aqueous medium. The solution is to choose a suitable support in which the catalyst can be dispersed, leading to a higher number of catalytically active sites. The variation in magnetic and photocatalytic properties with the increase in particle size as a function of CuO loading in the host KIT-6 presents an opportunity for deeper insight. The other area that calls for in-depth exploration is whether the mesoporous matrix (here KIT-6) plays a direct role in the photocatalytic process or merely serves as a support or host for CuO nanoparticles. The alteration in the electronic properties due to particle-size confinement in the nanometer regime will definitely alter several properties such as the band gap, valence band potential, surface charge, *etc*., which are very important parameters in the surface heterogeneous catalytic reaction in the solid and liquid phases. The choice of the SiO_2 mesoporous matrix is more important as it will not hamper the magnetic properties of these materials. However, in the present work, the effect of the CuO nanoparticles dispersed in KIT-6 on its photocatalytic efficiency and magnetic properties is studied.

2. Experimental (materials and methods)

2.1. Synthesis

a. Synthesis of mesoporous KIT-6. Ordered mesoporous SiO_2 (KIT-6) was synthesized using the triblock copolymer P-123 structural template and tetraethyl *ortho*-silicate (TEOS: $C_8H_{20}O_4Si$) as the source for silica using the hydrothermal method. Initially, the requisite amount of Pluronic P-123 was taken in distilled water and hydrochloric acid (37%) (ratio 20 : 1) was added to it and the mixture was continuously stirred for an hour. Thereafter, 5 g of *n*-butanol (99%) was added to the solution at 35 °C with continuous stirring. The stirring was continued for an hour and then 12.89 g of TEOS was added to the solution, and the mixture was continuously stirred at this temperature for 24 h. The sample was hydrothermally treated at 100 °C for another 24 h in an autoclave cell under static conditions. The white precipitate formed was collected using vacuum filtration and dried at 100 °C for 1 day. Thereafter, it was calcined at 550 °C for 6 h. The final product that was obtained was labelled as CK-0.

b. Synthesis of different weight percentages of CuO dispersed in KIT-6. CuO was dispersed in KIT-6 in 1, 5, 10 and 15 wt% with respect to KIT-6. The requisite stoichiometric amount of copper nitrate trihydrate was dissolved in water along with the required amount of KIT-6 and the resultant mixture was stirred at room temperature for an hour. Subsequently, water was removed by evaporation at 60 °C and the products that were obtained in each case were calcined at 350 °C for 2 hours and they were labelled as CK-1, CK-5, CK-10, and CK-15, respectively. This is described in Scheme 1.

A. Characterization. Phase analysis was carried out through powder X-ray diffraction (XRD) measurements using a Phillips Analytical diffractometer with Ni-filtered Cu K_α radiation. The diffractograms were recorded in the 10–70° (2θ) region. The

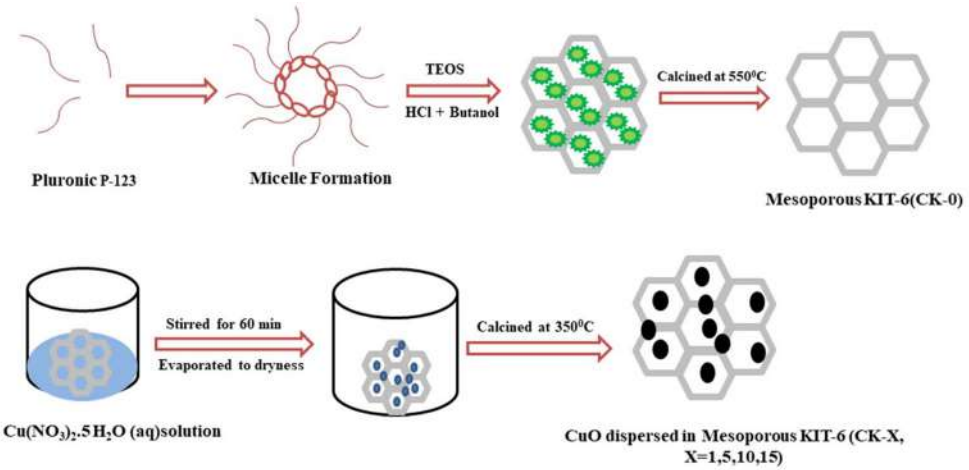

Scheme 1 Synthesis of different weight percentages of CuO dispersed KIT-6 nanoparticles.

BET surface area, pore volume, and pore size distribution profiles of different samples were obtained from physical adsorption of N_2 at 77 K, using a Micromeritics ASAP 2020 analyser. About 100 mg of the sample was utilized for this purpose, which was degassed under vacuum (10^{-6} Torr) at 300 °C, prior to N_2 adsorption. Small-Angle X-ray Scattering (SAXS) measurements were carried out using a laboratory-based SAXS instrument with Cu K_α as the probing radiation. The sample to detector distance was nearly 1 m. Radial averaged scattering intensity ($I(q)$) was obtained (where the wave vector transfer $q = 4\pi \sin(\theta)/\lambda$; λ is the wavelength and 2θ is the scattering angle) within a wave vector transfer range of ~0.1 nm^{-1} to 2.0 nm^{-1}. X-ray Photoelectron Spectroscopy (XPS) studies were performed using an SPECS instrument with a PHOBIOS 150 Delay Line Detector (DLD) employing an Mg K_α (1283.64 eV) dual anode as the X-ray source (power: 250 W, voltage: 10.00 kV, sample current: 175.6 nA) at a pass energy of 40 eV. As an internal reference for the absolute binding energy, the C-1s peak (284.5 eV) was used. All the deconvolutions are made using the CASA software with a Voigt type peak having GL (30) without imparting any asymmetry. The baseline was made using the Shirley function. Magnetization measurements were carried out using a Vibrating Sample Magnetometer (VSM) (Oxford Instruments, UK). In this method, the sample was mounted in a cryostat and placed between two pick-up coils. The sample was then magnetized in a uniform magnetic field and then sinusoidally vibrated with a certain frequency through the use of a piezoelectric material. A voltage is induced in the pick-up coil due to the change in the magnetic flux, proportional to the sample's magnetic moment. The magnetization curve of the sample was also recorded by sweeping the magnetic field. The DC-magnetization measurements were carried out as a function of temperature and magnetic field. Small angle XRD was performed on a Rigaku SmartLab XRD instrument with a θ–θ geometry (Bragg–Brentano) from θ = 0–5° with a scan speed of 2.5 and a step size of 0.02. UV–visible measurements in the 200–800 nm region were performed using a two-beam spectrophotometer (V-670, JASCO) with a diffuse reflectance (DR) attachment, employing barium sulphate-coated integration spheres as a reference. Steady state EPR was recorded on an X-band Bruker EMX 300 spectrometer. A total of 5 mg of the catalyst was taken in the EPR tube and the EPR was recorded at RT under a liquid N_2 atmosphere at a temperature of 120 K. Zeta potential measurements were performed at 25 °C using a quartz cuvette with a Malvern Zetasizer nanoseries, employing phase analysis light scattering with an applied field strength of 2.5×10^3 V m^{-1} and a He–Ne laser (632.8 nm) operating at 4.0 mW as the light source. About 0.5 mg mL^{-1} of the sample was dispersed in 1 mL of water. Scanning Transmission Electron Microscopy (STEM) of the powder samples was carried out at 300 kV using a JEOL GRAND ARM G^2 microscope, fitted with an EELS spectrometer with a Gatan Continuum EELS Filter. The energy dispersion of the EELS measurements was 1.5 eV per channel and the energy resolution was 0.9 eV. To prepare the samples, the powders were dispersed in IPA and dropcast on holey carbon coated 400-mesh Ni-grids (from Ted Pella Inc.). For superoxide trapping, about 2 mg of the photocatalyst was dispersed in 500 μL of water and the liquid was ultrasonicated for an hour and then 5 μL of 5,5-dimethyl-1-pyrroline *N*-oxide (DMPO) was added to the mixture, which was then taken in a capillary for free radical measurements at room temperature. The EPR spectra were recorded at room temperature using an X-band Bruker EMX 300 spectrometer, both in the presence of light and under dark conditions.

B. Photoelectrochemical measurements. The electrolyte was prepared with 0.1(M) KCl solution (Sigma Aldrich (99.5%) purity). For each photocatalyst 100 mg of the sample was dispersed in 1 mL isopropanol along with 30 μL Nafion (binder) and ultrasonicated for 30 min for uniform dispersion and the supernatant solution was drop-cast on a p-type silicon wafer (ρ = 1–10 Ω cm) which was dried at 60 °C for 2 h and this was used as the working electrode. Prior to drop-casting, the silicon wafers were cleaned using Piranha solution

($H_2SO_4 : H_2O_2 = 3 : 1$) each time to prevent any form of cross-contamination. The drop-cast silica wafer was used as the anode and the Pt wire coil was used as the cathode (counter electrode) and the Pt wire was used as the reference electrode. The electrochemical cell was connected to the Potentiostat/Galvanostat 2273 to perform chrono-amperometric switching studies at a bias of −1.5 V. The cell was irradiated using 1.5 AM sunlight type radiation from a solar cell testing system, Optosolar.

Using different CK catalysts, the degradation study of *o*-DCB was carried out. The photocatalytic reactor used was a cylindrical Pyrex glass reactor for photocatalytic degradation experiments. The reactor was irradiated with either a medium-pressure mercury lamp or a white light source. As a reaction condition, 60 ml aqueous solution of *o*-DCB (3.3×10^{-5} mol d^{-1} m^{-3}) was used as a model pollutant. About 100 mg of the photocatalyst was dispersed in the solution, and the mixture was stirred and exposed to visible light. The analytical technique used to monitor the concentration of *o*-DCB was UV-visible spectrophotometry at a wavelength of 225 nm. As a result, different sets of CK-*X* (X = 1, 5, 10, and 15) catalysts demonstrated commendable photocatalytic activity for the degradation of *o*-DCB.

2.2. Electrospray ionization-mass spectrometry (ESI-MS) study

In this study, we conducted an experimental analysis of the CK-*X* set of catalysts to compare their photocatalytic activity for the oxidation of *ortho*-dichlorobenzene (*o*-DCB). This investigation is essential for understanding the reaction kinetics and identifying different intermediates formed during the oxidation of *o*-DCB, leading to the production of carbon dioxide, using a diverse set of catalysts. ESI-MS studies were carried out using a Thermofisher QExactive orbitrap mass spectrometer equipped with an electrospray ionization (ESI) probe as the ion source. The mass of the molecules was determined in the form of *m*/*z* by injecting directly at a flow rate of 10 μL min^{-1} in the positive mode. The samples were introduced into the system after diluting in a concentration range of 2–10 μM using LC-MS grade water and filtered using a 0.2-μ filter. The capillary temperature (for de-solvation) was maintained at 150 °C with an auxiliary gas heater temperature of 100 °C and the spray voltage was maintained at 2 kV due to instability of species at elevated temperatures and spray voltages. The AGC target was 1e6 with five microscans and the maximum injection time was 50 ms. Data acquisition was performed for two minutes.

For the *ex situ* ESI-MS study, 60 mL *o*-DCB aqueous solution with a molar concentration of 3.3×10^{-5} M was added to a beaker and each photocatalyst (100 mg) was added. The photocatalytic system was initially stirred for 20 min at 200 rpm in the dark to disperse the powders for the adsorption analysis. Subsequently, the systems were exposed to visible light. At every 60-minute interval, an aliquot of *o*-DCB solution was taken out and added to the aqueous solvent to make the final concentration of 5 μM and the corresponding peaks were measured using an *ex situ* ESI-MS instrument. The same stirring procedure was repeated for the other mixtures, with the ESI-MS peak appearing after 10 minutes of stirring.

2.3 *Ab initio* calculations

Quantum chemical calculations were performed using density functional theory. Here, the Vienna *ab initio* simulation package (VASP)[36] electronic structure code was used along with the projector augmented wave (PAW) package.[37] Geometry optimization was carried out by relaxing both cell parameters and ionic positions under the framework of generalized gradient approximation (GGA) using the Perdew–Burke–Ernzerhof (PBE) functional,[38] Brillouin zone sampling had been carried out using the Monkhorst and Pack scheme[39] with a *k*-point mesh size of 5 × 4 × 1.[40] Self-consistent iteration was continued until energy convergence reached 10^{-7} eV. The $E_{cut\text{-}off}$ value was kept fixed at 500 eV throughout the calculation. The bulk calculation for CuO was performed using ICSD-26715 which matches the CuO bulk structure, as shown in Fig. 1B. Both spin orbit coupling and relativistic corrections were considered. The Unrestricted Density Functional Theory (UDFT)[41] was used to calculate band gap and magnetic properties. The hybrid functional of Heyd–Scuseria–Ernzerhof-2006 (HSE-06)[42] was used for calculating the magnetic effect and band gap. For magnetic and band gap with UDFT and HSE-06 spin–orbit coupling is used.

2.4 *In situ* FT-IR studies for pyridine and CO_2 adsorption

In situ FT-IR adsorption was performed in the DR-IR mode using the Harrick Praying Mantis cell. Initially an air background was recorded under a vacuum of 2×10^{-5} mbar. The sample was taken in the powder form and the sample treatment was undertaken as a function of temperature up to 150 °C. The resolution used was 4 cm^{-1}, 300 co-added scans for the sample spectra and 60 co-added scans for the background spectra. The aperture used was 0.5 mm with a Blackman–Harris apodization function. The sample was kept at 150° for 30 min and brought back to room temperature. A background with this treated sample was initially taken, followed by the introduction of adsorbed pyridine produced in a glass bulb. The spectra of the pyridine are shown in Fig. S11. The CO_2 adsorption was similarly done with CO_2 gas of 99.9% purity.

3. Results and discussion

A. X-ray diffraction (XRD)

Low angle X-ray diffraction (LXRD) patterns for KIT-6 and CuO dispersed in KIT-6 are presented in Fig. 1A. The LXRD pattern of KIT-6 (Fig. 1A(a)) exhibit a well-distinguished diffraction peak corresponding to the (2 1 1) plane and a hump for the (2 2 0) plane correspondingly at (0 to 5)° which is consistent with the earlier literature.[43–46] The synthesised KIT-6 shows the typical characteristic of an ordered cubic *Ia3d* symmetric mesoporous structure with a well-ordered cubic array. The cubic *Ia3d* symmetry in the synthesised samples majorly confirms that the reciprocal of the *d*-spacing for KIT-6 (CK-0) pre-

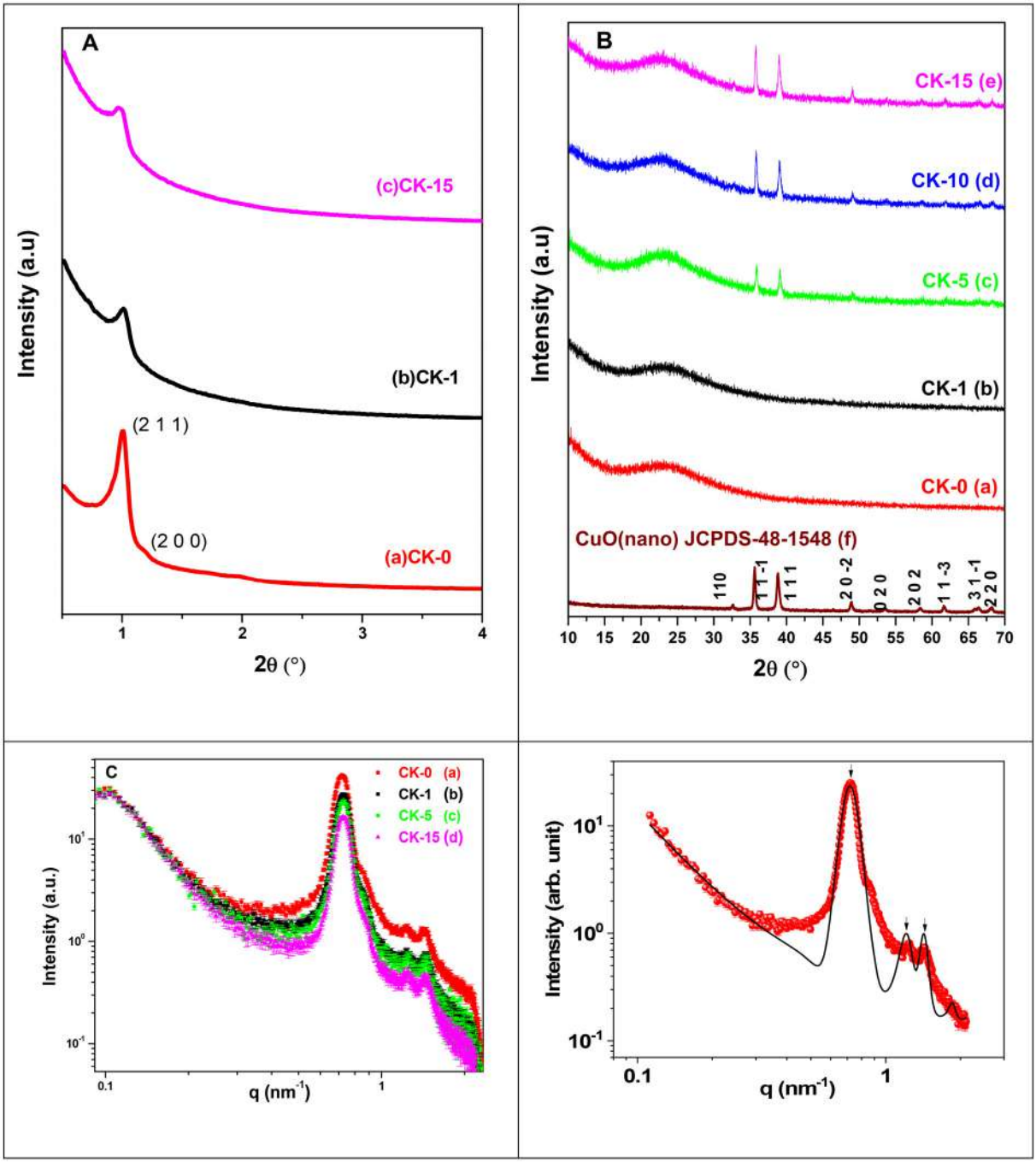

Fig. 1 (A) Low angle X-ray diffraction data for different CuO dispersed samples in mesoporous KIT-6 (a) CK-0; (b) CK-1; and (c) CK-15. (B) X-ray data from (θ = 10° to 70°) for the samples (a) CK-0; (b) CK-1; (c) CK-5; (d) CK-10; and (e) CK-15. (f) CuO-synthesised. (C) Small-angle X-ray scattering data for the sample- (a) CK-0; (b) CK-1; (c) CK-5; and (d) CK-15. (D) Fitting of the canonical 2-D hexagonal lattice model to the small-angle X-ray scattering data.

pared at 550 °C has a linear relationship with the square root of the sum of h^2, k^2, and l^2. However, as a function of the dispersion of CuO in the synthesised CK-0 matrix there is a considerable reduction in the intensity of the (2 1 1) plane for CK-1 followed by CK-5. This indicates that CuO may have been incorporated into the cubic channel arrays of the KIT-6 matrix thereby lowering the *d*-spacing and in turn lowering the intensity of the major LXRD peak. The understanding of pore filling will be further extended in the SAXS section in greater detail.

The indexed XRD pattern for the synthesised CuO nanoparticles (Fig. 1B(f)) matches the monoclinic structure (JCPDS 48-1548) with no impurities found and is denoted here as bulk CuO. CK-15 also possesses all the major peaks present in bulk CuO, which points towards the presence of CuO over the

surface along with that of the CuO nanoparticles present in the pore channels of KIT-6. CK-1 does not have any participation from the CuO bulk peaks, showing that the majority of CuO molecules are present in the pore channels and a smaller number of CuO molecules is present over the surface. However, in CK-5 the presence of certain CuO peaks confirms a certain extent of CuO deposition on the surface along with the hexagonal pores of KIT-6. This will be further explained in the Morphological and crystallographic studies section.

B. Small-angle X-ray scattering (SAXS)

SAXS analyses were performed to quantify structural correlation and pore filling. Radially averaged scattering intensity, $I(q)$, was recorded as a function of the wave vector transfer q, defined by eqn (1a):

$$q = \frac{4\pi \sin\theta}{\lambda} \quad (1a)$$

where λ is the X-ray wavelength and 2θ is the scattering angle. Measurements were conducted over a q-range of ~0.1 to 2.0 nm^{-1}. Scattering profiles were analyzed using a polydisperse cylindrical shell model using the open software SASFit.[37]

SAXS data, normalized at the lowest q value, are shown in Fig. 1(C). From the scattering profile, a strong correlation peak owing to correlated mesopores is observed at q ~0.71 nm^{-1}. The highly reduced second and third peaks are observed at 1.23 and 1.45 nm^{-1}, respectively. This indicates the peak position ratios of $1:\sqrt{3}:2$. It should be noted that a canonical 2D hexagonal lattice, such as the one formed by hexagonally packed cylinders, exhibits peak positions in this order. Furthermore, it is observed that the peak height significantly decreases once CuO is incorporated into the structure.

The following model was used to analyze the data of KIT 6 using software SASFit.[47]

Total scattering intensity $I(q)$ can be represented as given in eqn (1b):

$$I(q) = C\left\langle \int_{R_{min}}^{R_{max}} F^2(q, L, t, R)V^2D(R)\mathrm{d}R \right\rangle S(q) \quad (1b)$$

where $F(q, L, t, R)$ represents the form factor of a long cylindrical shell with length L, shell thickness t and core radius R and volume V. $S(q)$ represents the structure factor of such hexagonally ordered objects.

$D(R)$ represents the particle size distribution, *i.e.*, $D(R)\mathrm{d}R$ is proportional to the probability of having size between R and $R + \mathrm{d}R$. In the present case standard lognormal distribution is considered, as given by the following equation.

$$D(R) = \frac{1}{\sqrt{2\pi\sigma^2R^2}}\exp\left[-\frac{[\ln(R/R_0)^2]}{2\sigma^2}\right] \quad (2)$$

R_0 represents the mean radius and σ represents the spread of the distribution obtained by fitting the above model with the SAXS profiles. The fit of the above model is depicted as the solid line in Fig. 1D. The R_0 obtained for KIT-6 is 2.78 ± 0.01 nm, where σ has a value of 0.133 and a shell thickness-t 2.9 nm, with the cylindrical shell L of >50 nm. The inter-pore lattice constant is 10.19 ± 0.01 (nm). It is observed that the peak height of the profile at q ~0.71 nm^{-1} decreases after incorporating 1 wt%, 5 wt% and 15 wt% CuO by 1.53, 1.79 and 2.63 fold, respectively, although the position of the peak in each case remains more or less unchanged. This indicates that the pores get filled without affecting the pore size or pore ordering. If the ϕ fraction of the pore gets filled, then the new scattering contrast is $(\rho_{silica} - \phi\rho_{CuOX})^2$ where the initial scattering contrast is ρ_{silica}^2. Here, ρ_X denotes the scattering length of compound X. Thus, the ratio of $\rho_{silica}^2/(\rho_{silica} - \phi\rho_{CuOX})^2$ should be equal to the decrease in the intensity of the peak.

Assuming the density of SiO_2 and CuO as 2 g cm^{-3} and 6.31 g cm^{-3}, and considering CK-1, CK-5 and CK-15, the following values were obtained. The scattering length density for SiO_2 (KIT-6/CK0) is 1.88×10^{11} cm^{-2}; and those for others are CK-1 – 1.9271×10^{11} cm^{-2}; CK-5 – 2.1158×10^{11} cm^{-2} and CK-15 – 2.5875×10^{11} cm^{-2}. Table 1 shows the fraction of the pores filled in the parent KIT-6 mesoporous silica by the dispersion of CuO.

Therefore, it is quite apparent that as a function of CuO impregnation in KIT-6 the pores of KIT-6 get filled to different extents, as shown in Table 1.

C. N_2-adsorption and pore size

The measurement of the textural properties of as-synthesized materials is accomplished using nitrogen adsorption/desorption measurements, which were used to calculate the specific surface area, pore size distribution, and specific pore volume

Table 1 Fraction of the pores filled in the parent KIT-6 mesoporous silica by dispersion of CuO in KIT-6

Sample name	ϕ
CK-1	0.34
CK-5	0.39
CK-15	0.45

Table 2 Textural, morphological and catalytic properties for different photocatalysts

Sl. no.	Sample	Surface area[a] ($m^2\ g^{-1}$)	Pore size[b] (nm)	Particle size[c] (nm)	Band gap[d] (eV)	Rate constant[e] (min^{-1})
1	CK-0	676	6.9	—	4.53	
2	CK-1	665	5.56		2.86	4.09×10^{-4}
3	CK-5	590	5.48	5	2.77	13.28×10^{-4}
4	CK-10	576	5.47	7	2.65	37.94×10^{-4}
5	CK-15	450	5.39	9	2.59	21.36×10^{-4}

[a] Obtained from the BET surface area. [b] Obtained from the desorption BJH curve. [c] Calculated from the HRTEM/STEM morphologies. [d] Calculated from the DR-UV-Vis studies. [e] Calculated from the photocatalytic degradation of *o*-DCB (discussed in the Photocatalytic activity section).

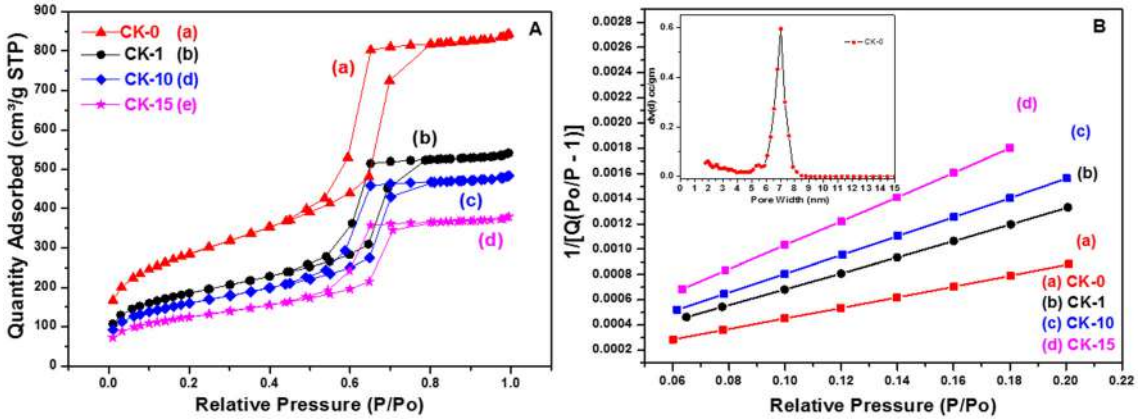

Fig. 2 (A) Adsorption isotherm plot for all the different samples of CuO dispersed in the KIT-6 matrix; (B) BET-isotherm plot for the different samples and the inset has a typical pore size distribution plot from the desorption BJH curve for the samples: (a) CK-0; (b) CK-1; (c) CK-10; and (d) CK-15.

of KIT-6 and CuO dispersed in KIT-6 materials, as shown in Table 2. All the samples display Type IV isotherms (Fig. 2A). The presence of a sharp capillary condensation or evaporation at higher relative pressure and H1 hysteresis loop indicates that all the materials have a uniform pore structure with large channel-like mesopores. CK-0 (KIT-6) shows the largest specific surface area, pore volume and mean pore diameter [Fig. 2B (inset)] of ~7 nm.

Compared with that of KIT-6, for the other photocatalysts CK-1, CK-5, CK-10 and CK-15, the pore diameter, specific surface area and total pore volume show a decreasing trend. The specific surface area decreases with increasing amount of CuO dispersed in KIT-6 which can be explained by the pore plugging inside mesoporous channels due to the assembly of some non-uniform sized nanocrystals of CuO in the pore channels of CK-0, as has been observed in the literature for different mesoporous matrices.[39,48] Different pore sizes (Fig. S5) also show a reducing trend with increasing CuO dispersion in KIT-6 also, implying filling of the pore channels of the as synthesised KIT-6 by the CuO nanoparticles which is explored previously in the SAXS section.

D. Morphological and crystallographic studies (STEM, HRTEM and EELS study)

KIT-6 is mesoporous silica consisting mainly of a three-dimensional network of interconnected pores and can be described generically as possessing a cubic *Ia3d* structure. One of the major methods used to substantiate the ordered pore structure of KIT-6 is High-Resolution Transmission Electron Microscopy (HRTEM), revealing the highly ordered arrangement of its mesopores. Fig. S7 shows the HRTEM image of the synthesised KIT-6 showing the highly ordered channel with well-ordered cubic array pores along the (2 1 1) plane, as shown previously in the literature.[34–36]

The HRTEM image shows a definite *d*-spacing of 0.25 nm, matching with the (2 1 1) present in KIT-6. Once CuO is dispersed in the KIT-6 matrix at different amounts, the CK-5 photocatalyst possesses the particles within the pore channels of KIT-5. CK-5 (Fig. 3A) mainly shows that the CuO particles are present mainly within the pore channels. Almost no CuO particles are present outside the pore channels on the surface, as can be observed in both Fig. 3A and B. The STEM image for CK-10 (Fig. 3C) shows that the particles are mainly present within the pore channels as well as on the surface, which is in accordance with the XRD data, as studied earlier. The CK-15 sample also shows that the CuO particles are present both inside the pore channels and on the surface. As the particle size is calculated for the different samples, as shown in the inset of Fig. 3, the variation is observed among CK-5 (~5 nm), CK-10 (~7 nm) and CK-15 (~9 nm). CK-1 is likely to have a smaller particle size. The elemental mapping (Fig. 4A) of the pore channels clearly shows the presence of copper (Fig. 4B) and oxygen (Fig. 4C) in a stoichiometric amount. The EELS mapping for similar particles (Fig. 4D) present in the pore channels of CK-15 and the representative EELS edge plot for Cu L-edges of Cu standard data and CuO impregnated KIT-6 (Fig. 4E) clearly shows the presence of CuO.

E. Diffuse reflectance UV-visible (DRS-UV-Vis) spectroscopy

The Diffuse Reflectance Spectroscopy (DRS) study for the CK samples is shown in Fig. 5A. It was found that the band gap changes as a function of CuO dispersion over KIT-6. With the increase in the CuO concentration in KIT-6, DRS plots show a distinct red shift as compared to bare KIT-6. Apart from KIT-6 all the catalysts possess band gaps in the visible region. An estimate of the optical band gap energy (E_g-gap) was obtained from a plot of the Kubelka–Munk function $F(R)$ as given in eqn (3):[49]

$$F(R) = A(h\nu - E_g)^{m/2} \quad (3)$$

where $h\nu$ is the photon energy and m is a constant that depends on the nature of optical transition. The Kubelka–Munk plots of these materials are depicted in Fig. 5A(a–e). With decreasing amount of CuO in the host moiety, the band gap value becomes higher mostly due to the quantum confinement effect. The different band gap values of the CK samples are reflected in Table 2.

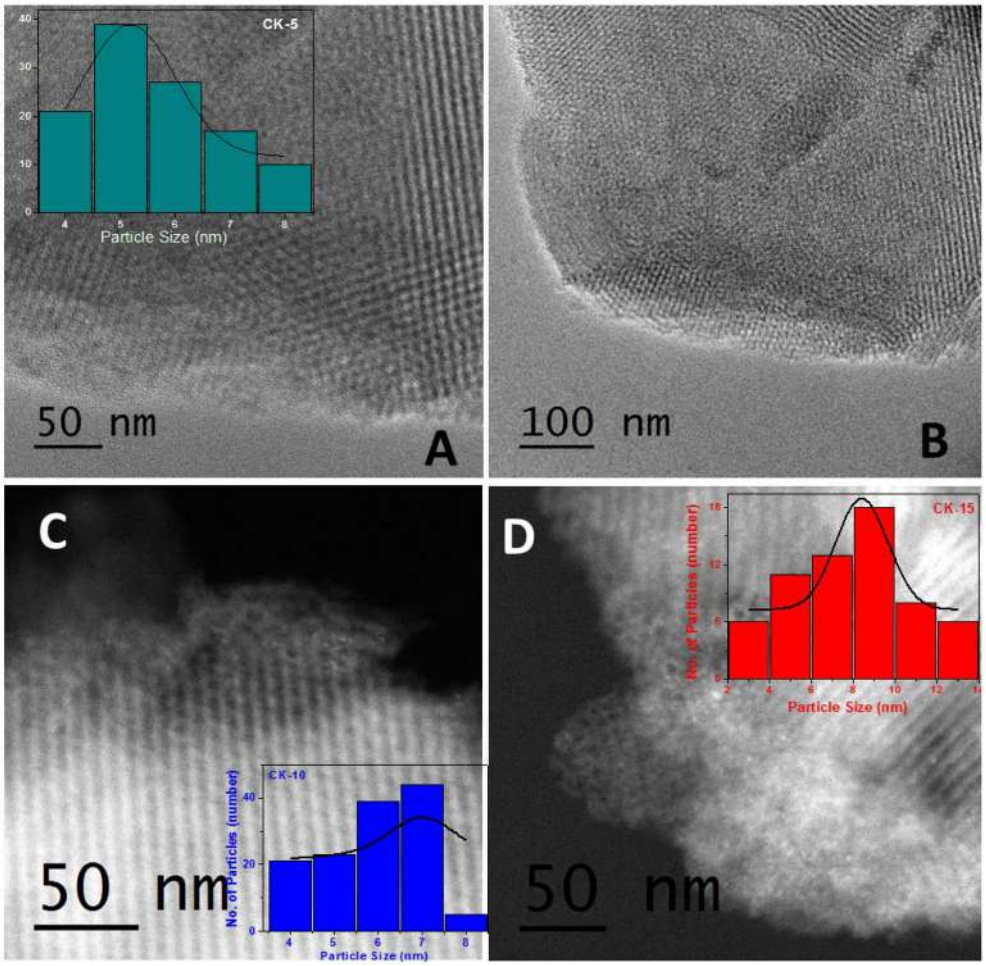

Fig. 3 STEM and HRTEM images of the samples (A) CK-5 (scale-50 nm); (B) CK-5 (scale-100 nm); (C) CK-10 (scale-50 nm) and (D) CK-15 (scale-50 nm). The inset shows the histogram showing the variation in the particle size.

A. Photovoltaic switching experiment and Mött–Schottky plots

Photoelectrochemistry is an important method to monitor the complex photocatalysis steps such as charge generation, separation and migration to reactive species. The reusability of the photocatalyst is a deciding factor for the practical applications of a photocatalyst. As shown in Fig. 5C the switching experiments show the reusability of the photocatalysts and the photocurrent generated by these photocatalysts.

Mott–Schottky (MS) analysis has become widely adopted to estimate the key operational parameters of semiconductor photoelectrodes, namely, the flat-band potential, E_{fb}, and the donor concentration, N (for an n-type semiconductor photoanode), or acceptor concentration, N_a (for a p-type photocathode). The Mott–Schottky relationship involves the apparent capacitance measurement as a function of potential under depletion conditions eqn (4):

$$\frac{1}{C^2} = \frac{2}{e\varepsilon\varepsilon_0 N}\left(E - E_{fb} - \frac{kT}{e}\right) \quad (4)$$

where C = capacitance of the space charge region; ε = dielectric constant of the semiconductor; ε_0 = permittivity of free space; N = donor density (electron donor concentration for an n-type semi-conductor or hole acceptor concentration for a p-type semiconductor); E = applied potential; E_{fb} = flatband potential; k = Boltzmann constant; T = temperature; and e = electronic charge.

The donor density can be calculated from the slope of the $1/C^2$ *vs.* E curve, and the flat band potential can be determined by the extrapolation to $1/C = 0$.

In the Mott–Schottky analysis, a plot of $1/C^2$ *versus* the applied potential (E) provides insight into the semiconductor type and its electronic properties. A negative slope in this plot indicates p-type conductivity, characteristic of hole-dominated charge transport. Conversely, a positive slope signifies n-type conductivity, associated with electron-dominated transport. The extrapolation of the linear region to the intercept at $1/C^2 = 0$ yields the flat band potential (V_{fb}) of the material.

As shown in Fig. 5B, the photocatalysts CK-1 and CK-5 possess a negative slope and therefore, can be treated as pure p-type photocatalysts. However, for CK-10, CK-15 and the bulk photocatalysts possess both positive and negative slopes

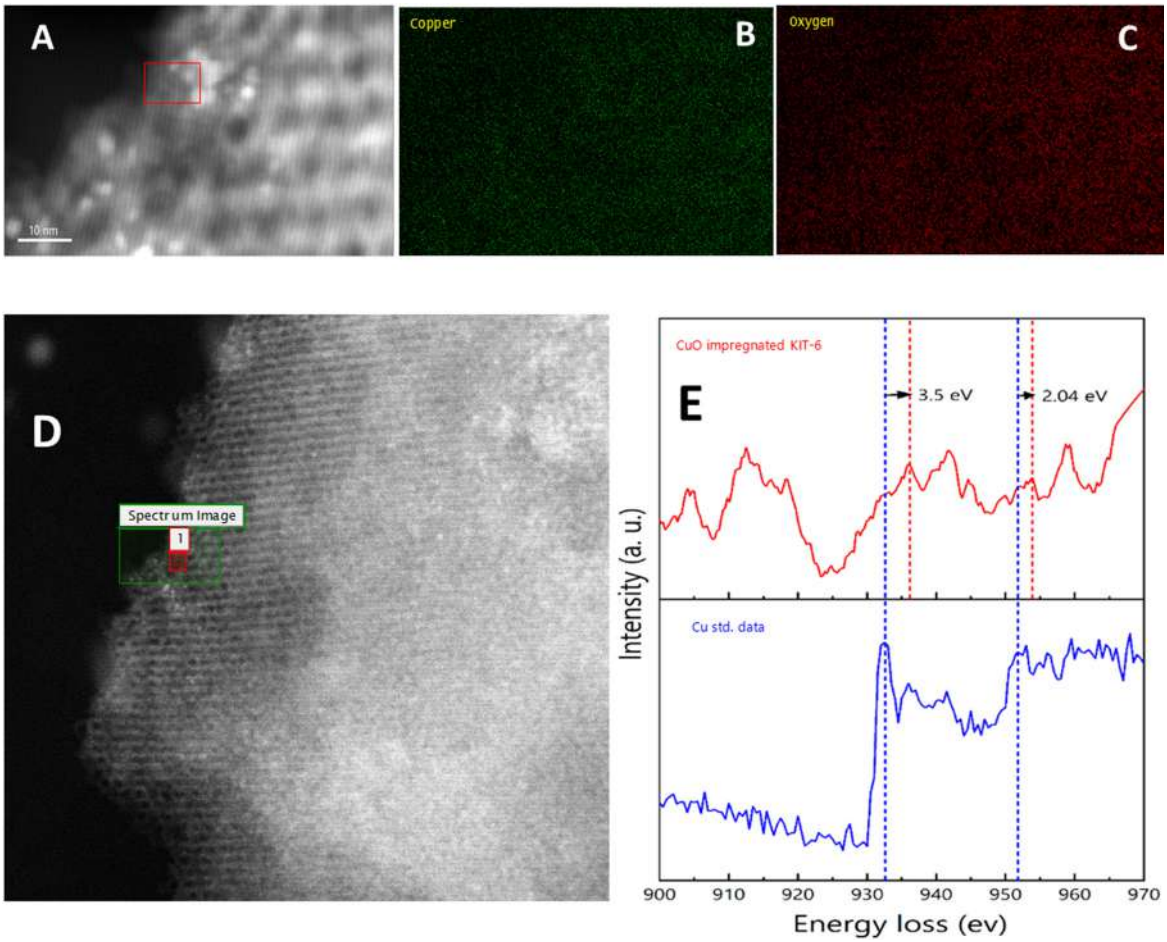

Fig. 4 (A) STEM and (B) elemental mapping showing the presence of Cu. (C) Elemental mapping showing presence of O in the CK-15 sample. Inset shows the position prom which the elemental mapping is obtained. (D) STEM image showing the CuO particles within the pore channels of KIT-6 for the CK-15 sample used for the EELS mapping and (E) EELS edge plot for Cu L-edges of Cu standard data and the CuO impregnated KIT-6.

making a p–n type heterojunction. However, as these materials like KIT-6 will be having different Fermi energies therefore these materials are entirely different and the value of their "ε" and "ε_0" are also different, therefore the slope value of each of them won't exactly relate to the respective comparison of their donor density (N). However, the flat band potential (E_{fb}) has been calculated for all these systems from the intercept of eqn (4). The valence band potential can be calculated from E_{fb} by converting E_{KCl} (0.1 M) to SHE (pH = 7), then to SHE (pH = 0) and finally to vacuum

(1) E_{KCl} (0.1 M) to SHE (pH = 7) = 0.2881 V.
(2) SHE (pH = 7) to SHE (pH = 0) = 0.414 V.
(3) SHE (pH = 0) to vacuum = 4.4 V (vacuum).

So valence band potential,

$$E_{VB} = [E_{fb} + (0.414 + 0.2881 + 4.4)]V = (E_{fb} + 5.1021)V \quad (5)$$

$$E_g = (E_{VB} - E_{CB})V \quad (6)$$

So,

$$E_{CB} = (E_{VB} - E_g)V \quad (7)$$

The values of E_{VB}, as calculated from the Mott–Schottky plots, are given in Scheme 2.

The valence band potential for KIT-6 is maximum (3.62 eV) and the value decreases as a function of CuO- dispersion in the KIT-6 matrix as presented in Scheme 2.

The valence band potential obtained from the flat band potential is portrayed in Scheme 2 along with the conduction band potential calculated from the band gap and the valence band potential. As a function of dispersion of CuO in the KIT-6 matrix, there is an alteration in the particle size, and in turn, an increase in the particle leads to changes in the valence band potential and the conduction band potential. The valence band potential for CK-15 is 4.921 eV and that of CK-1 is 4.71 eV. The valence band potential for bulk CuO is found at a lower value of 4.66 eV. This will have a strong effect on their oxidation properties in the photocatalytic degradation of *o*-DCB as studied later.

The band gap of the bulk CuO is 2.44 eV and the comparative band gap, as obtained from HSE-06 DFT, is 2.3 eV, as shown later.

The photovoltaic switching (switch-on/off experiments) behaviours of the synthesized catalysts, encompassing

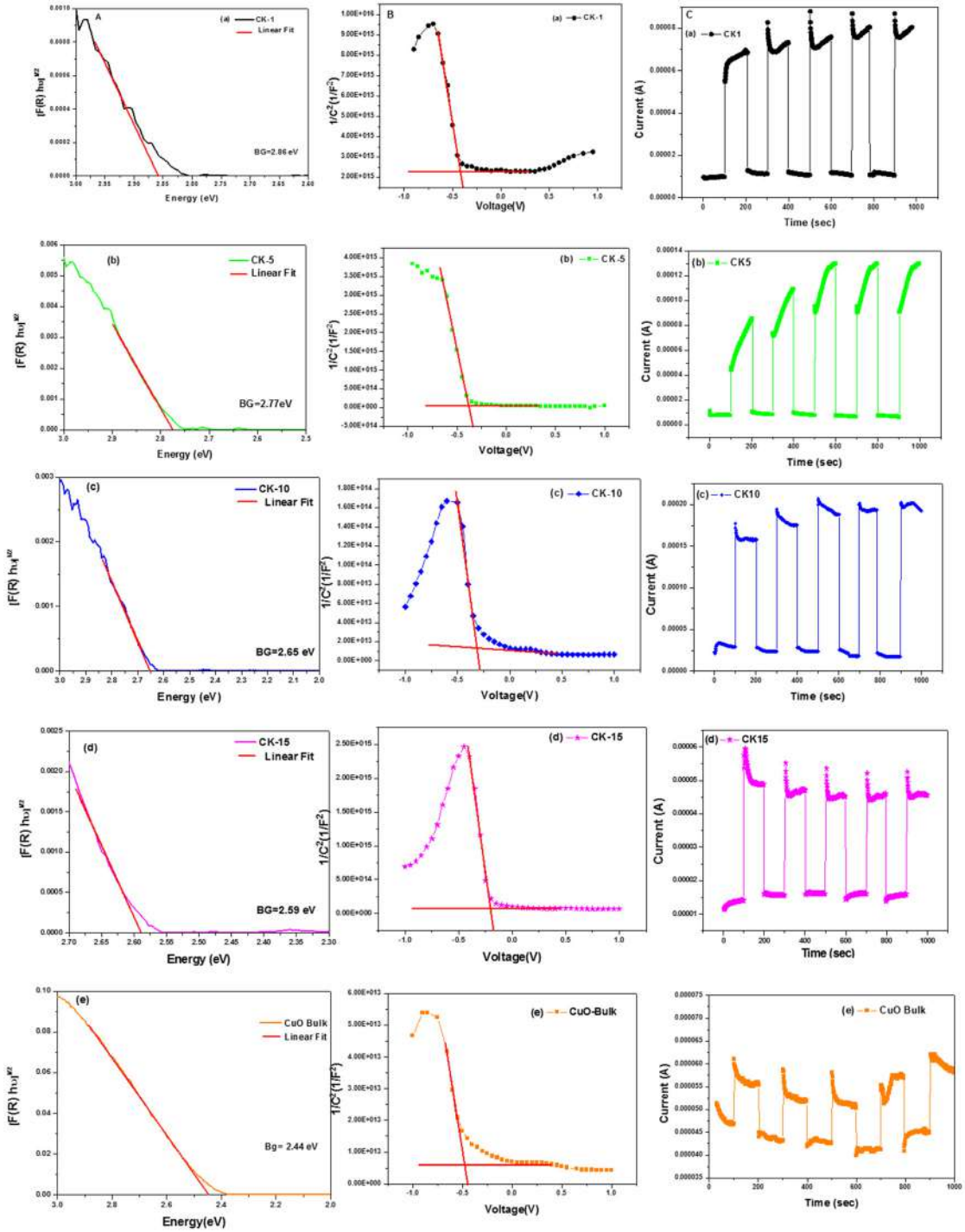

Fig. 5 (A) UV data, (B) Mött–Schottky data and (C) photovoltaic switching experimental data for the samples (a) CK-1; (b) CK-5; (c) CK-10; (d) CK-15; and (e) CuO Bulk.

CuO and CK-0 to CK-15 were investigated to elucidate their photoresponsive properties, directly relevant to their photocatalytic efficacy. The cyclic current–time plots (Fig. 5C) demonstrate a clear and reversible resistive switching behaviour across all samples, indicating the material's ability to generate and modulate photocurrent upon visible light irradiation. The photoswitching experiments show that CK-10 has the maximum photocurrent density as compared to the rest of the samples. Primarily the photoresponse current of all the CK catalysts except CK-0 are better as compared to that of CuO. The CK-10 photocatalyst shows the maximum photoresponse current amongst all the photocatalysts, which is expected to significantly enhance its photocatalytic activity.

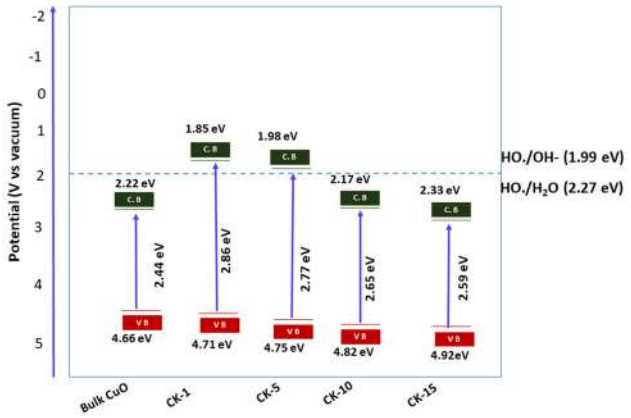

Scheme 2 The valence band potentials, conduction band potential and the band gap for the different samples along with bulk CuO.

B. Zeta potential studies

The zeta potential serves as a crucial parameter for finding the effective surface potential established by an electrical double layer at the interface between nano-CuO and CuO in KIT-6 (CK-0 to CK-15) photocatalysts in a solvated aqueous environment. The photocatalytic degradation of *o*-DCB in water is basically a manifestation of the solid–liquid interphase reaction. Therefore, the photocatalytic processes of either or both adsorption and formation of the intermediates and desorption of the subsequent products will strongly depend on the surface charge of the photocatalysts. The zeta potential values for different CK photocatalysts as a function of varying pH conditions are depicted in Fig. 6A. At neutral pH (pH-7) all the photocatalysts show a negative surface charge (Fig. 6A), whereas CK-15 exhibits the most negative surface (Fig. 6A(e)) charge amongst all the photocatalysts. CK-0 (Fig. 6A(a)), *i.e.* the host KIT-6 also possesses a negative surface charge. At lower pH, there is more addition of H^+ to the system and generically the surface charge is expected to increase, which is reflected in the zeta potential of these photocatalysts. At acidic pH 4 all these photocatalysts possess a positive surface charge, including CK-0. At alkaline or basic pH (~pH 10), there is more amount of OH– on the surface and thereby the surface charge is expected to be more negative as compared to that at pH 7. Consistently all these photocatalysts possess more negative surface charge at ~pH 10 (Fig. 6A). This supports the trend observed with increasing pH.

C. *Ab initio* calculations

The formation energy was calculated as:

$$\text{Formation energy } (\Delta E)\ \text{eV} = \frac{\text{total energy} - \sum n \times \text{energy of each atom}}{\text{total number of atoms}} \quad (8)$$

The relaxed lattice structure is found to possess an oblique rhombic prism shape representing a monoclinic crystal system with $C2/c$ symmetry. The lattice parameters are a = 4.21, b = 3.93 Å, and c = 5.32 Å and angles are $\alpha = \beta = 90$ and $\gamma = 87.71$ (F). The isoelectronic plot shows the density of electrons over O and Cu possesses a positive charge. The band gap value, as optimized with the Hubbard (U) parameter value of Cu-3d as 7.15 (ref. 50) (up spin is 1.45 eV and down spin is 1.49 eV) matches with the present literature.[51] The magnetization parameter calculation with UDFT is 4.005μ_B. The band gap optimized using the HSE-06 method shows a value of 2.32 eV, which is presented in Table S2. The magnetization parameter, as calculated only with the PBE DFT functional, is 0. However, the magnetization parameter calculated by UDFT is 4.005μ_B for the unit cell of CuO with 4 atoms of Cu and 4 atoms of O. Similarly, the magnetization parameter calculation with HSE-06 is 4μ_B with a similar unit cell.

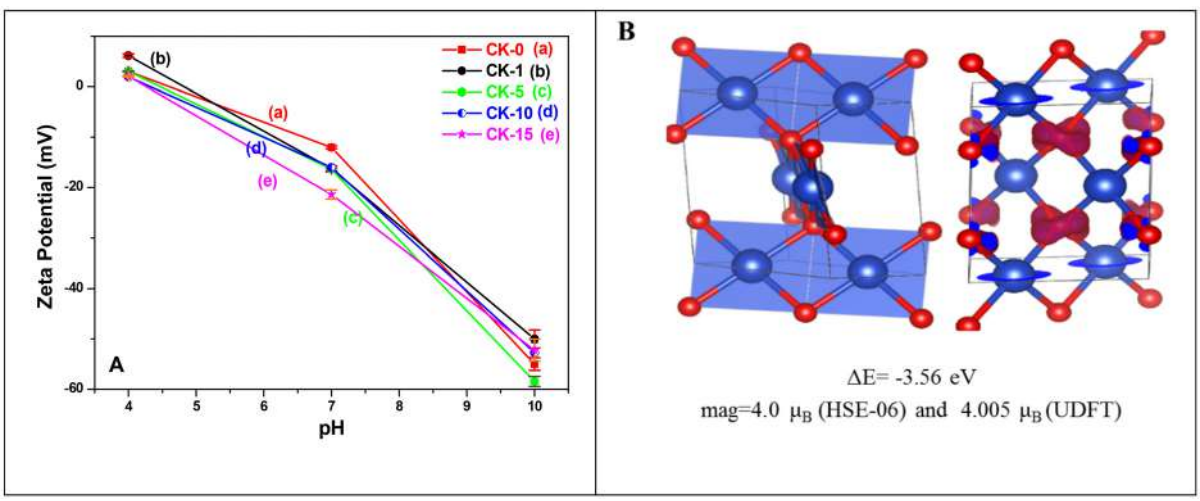

Fig. 6 (A) Zeta potential data for samples (a) CK-0, (b) CK-1, (c) CK-5, (d) CK-10, and (e) CK-15. (B) Ground state monoclinic CuO with its isoelectronic plot (ΔE = formation energy of CuO, mag = magnetic moment).

D. X-ray photoelectron spectroscopy (XPS)

The XPS spectra for the different photocatalysts were studied initially to understand the host (KIT-6) and the guest (CuO) moieties as a function of dispersion of these in the hexagonal channels of KIT-6 with which the electronic interaction between these host and the guest moieties can be inferred. The XPS dataset of Si-2p for the different samples (Fig. 7A) shows the presence of Si at 103.8 eV which is in conjunction with the earlier literature.[36,38] Essentially, there is no shift in the binding energy of Si as a function of CuO dispersion in the KIT-6 matrix [Fig. 7A(a–d)], showing minimal electronic interaction with that of the host KIT-6 matrix.

The XPS spectra of different photocatalysts showing the binding energy of O-1s (Fig. 7B) can be deconvoluted mainly into three peaks at 529.3, 530.4 and 532.0 eV, respectively. As these materials possess two types of compounds namely SiO_2 and CuO, the first peak could be attributed to the O-1s of CuO

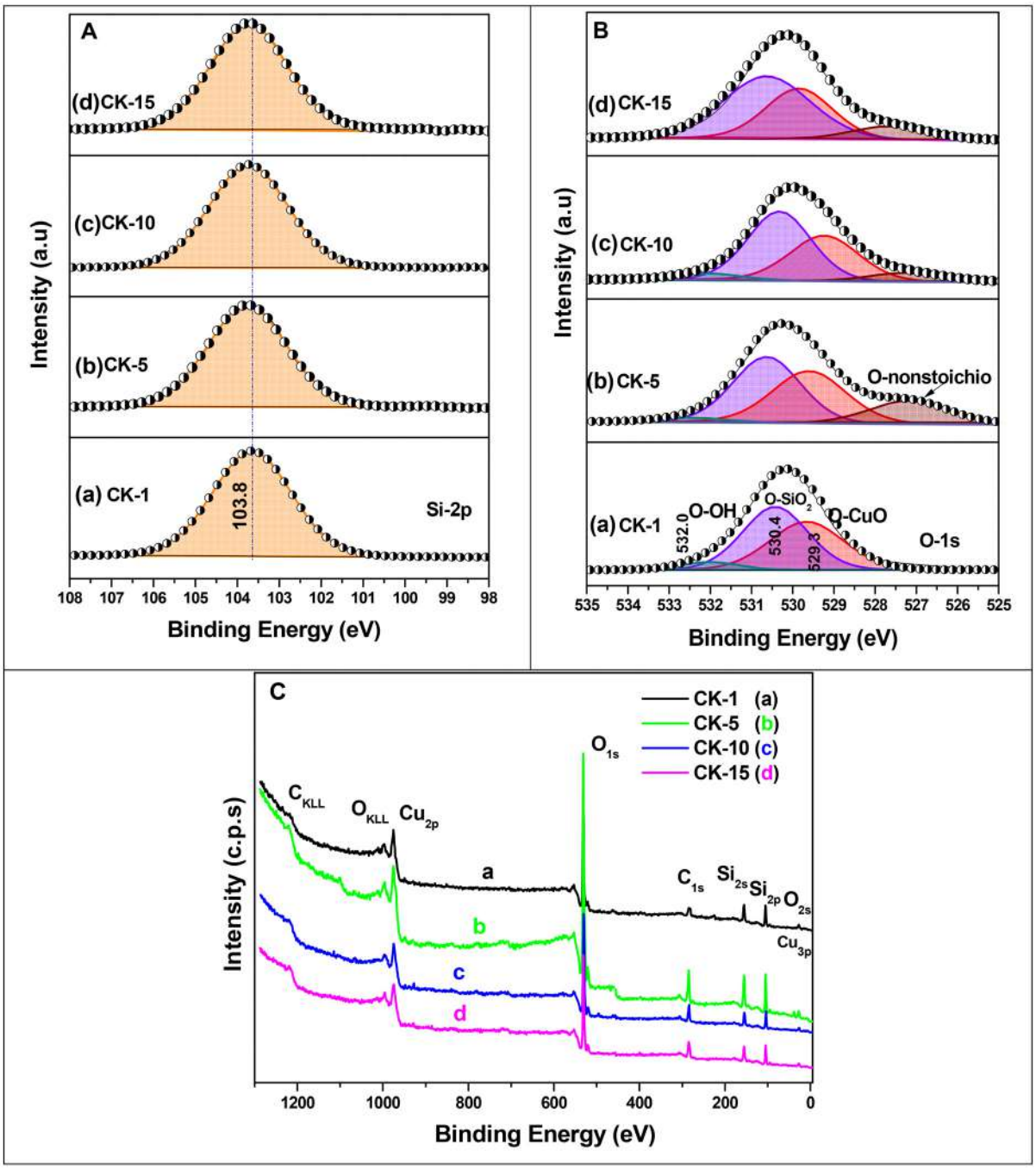

Fig. 7 Deconvoluted XPS data (A) Si-2p and (B) O-1s. (C) Survey scan for the different samples (a) CK-1, (b) CK-5, (c) CK-10 and (d) CK-15.

(Cu^{2+}); the latter one with higher binding energy can be attributed to the O of SiO_2 (Si^{4+}) and the final one to the O of surface –OH groups[52] that are attached with KIT-6. However, from CK-5 onwards, another peak appears at a lower binding energy of ~527.2 eV, which is usually attributed to O non-stoichiometry.[53,54] The binding energy for the peaks corresponding to O-(CuO) and O-(SiO_2) remains unaltered, showing lesser electronic interaction between the CuO nanoparticle guest molecules and the SiO_2 (KIT-6) host matrix. However, the intensity of the peak associated with O non-stoichiometry (527.2 eV) also decreases with increasing CuO dispersion. As it is quite evident that there are no O-vacancy peaks, and also the effect of excess O can be nullified, therefore, the effect of O non-stoichiometry mostly will result from the effect of O-frustration between the O of CuO and that of SiO_2, which is also negated with a higher concentration of CuO. As has been understood from the EELS plot, the CuO in the channels of KIT-6 mainly exhibits Cu^{2+}.

The XPS Cu-2p plots for the different samples (Fig. S4) mainly exhibit the presence of Cu^{2+} and there is complete absence of any Cu metal. The satellite peak at 937 eV is a signature of CuO nanoparticles. There is very less alteration in the binding energy of CuO as a function of CuO dispersion in the hexagonal channels of KIT-6, which implies that there is an interaction between the Cu of CuO and the O- of SiO_2. Therefore, CuO can be unequivocally designated as nanoclusters that do not exhibit any electronic interaction with that of host KIT-6, as has been observed earlier by Feng *et al.* with CuO-SBA-15.[55] However, there is a small amount of O-frustration between O- of CuO and that of SiO_2.

E. Electron paramagnetic resonance (EPR) measurements at 120 K

Electron paramagnetic resonance (EPR) was employed to further distinguish Cu species in different photocatalytic samples of CuO dispersed in KIT-6. EPR is a quite sensitive technique for the detection of tiny amounts of paramagnetic species. Cu^{2+} ions have an electronic configuration of d^9 and are paramagnetic over a wide range of temperatures. At room temperature, the observed resonance signal is assigned to the paramagnetic Cu^{2+} ions[56] at 3243 G. However, super-paramagnetism in CuO nanoparticles is observed when the particle size is reduced to the nanoscale. This phenomenon arises from the increased surface-to-volume ratio, leading to a greater contribution of surface effects to the overall magnetic properties. Smaller CuO nanoparticles exhibit uncompensated Cu^{2+} spins on the surface of the CuO nanoparticles, characterized by the absence of hysteresis at temperatures above the blocking temperature. When the particle size is small enough, the thermal energy can overcome the magnetic anisotropy energy, causing the magnetic moments to randomly flip direction. This results in the loss of hysteresis at temperatures above the blocking temperature[57,58] with caution where shape-anisotropy could also affect the magnetic moment along with size.[36] Fig. 8A shows the representative EPR signals for the CuO bulk and those of CuO dispersed over KIT-6. The CuO bulk signal matches with that of the literature[42] and as a function of the particle size in the CK-1 to CK-15, the paramagnetic EPR signal of Cu^{2+} increases as the particle size reduces. Mostly the paramagnetic effect increases with decreasing particle size which arises from the presence of uncompensated Cu^{2+} ions at the surface. The STEM and TEM studies effectively show the increase in particle size as a function of dispersion of CuO in the KIT-6 matrix. The particle size decreases from CK-15 to CK-1; however, the intensity of their EPR signal increases. Also, it is quite interesting to observe that as the particle size decreases, the FWHM for the paramagnetic EPR signal also decreases, indicating a decrease in the types of Cu^{2+} paramagnetic signals, and they are mostly attributed to the uncompensated Cu^{2+} spins present at the surface of the CuO nanoparticles.

F. Magnetism

CuO, being a transition-metal oxide, is mainly antiferromagnetic in nature as are the other oxides of the first d-orbital series.

CuO is distinctive in possessing a monoclinic unit cell with square-planer coordination of copper and oxygen. There are two distinct square planar bonds of Cu–O in the diagonal resulting in the unit cell to become an unstable monoclinic system.[59] Seehra *et al.* reported in their study that CuO NP's below 10 nm exhibit nanoparticle magnetism due to uncompensated surface spins resulting in a weak-ferromagnetic component. The weak magnetic behaviour is explained in terms of uncompensated surface Cu^{2+} spins, whereas the transition at 40 K is suggested to be the Néel temperature (T_N) of the spins in the core of nanoparticles.[60] Similar effects are also observed for the permalloy/CoO system.[49] Biju *et al.* reported lowering of the Néel temperature T_N with the particle size for CuO nanoparticles. As compared to the bulk the CuO nanoparticles possess a weaker super-exchange spin path for the Cu–O–Cu paths due to the presence of defects such as O^{2-} vacancies.[61] Similarly, Chen *et al.* reported the alteration in the magnetic properties for the CuO nanoparticles, around 13–17 nm particle size. They have observed the coexistence of paramagnetic surface contribution and that of antiferromagnetic behaviour in CuO nanoparticles. A correlation for the magnetic measurements for CuO nanoparticles, has effectively shown spin alteration due to the presence of uncompensated Cu^{2+} ions at the surface of the particles.[47] When the particle size is small enough, the thermal energy can overcome the magnetic anisotropy energy, causing the magnetic moments to randomly flip direction. This results in the loss of hysteresis at temperatures above the blocking temperature. The magnetic properties for the CuO nanoparticles observed at 5 K indicate that the particle size mostly plays a role in determining the magnetic behavior.

The morphological studies show that there are mainly two types of CuO: those in the mesopores of KIT-6 and those present on the surface, which exhibit the wide-angle XRD reflections and display a bulk structure. The previous XPS and the EELS mapping study shows mainly the presence of the

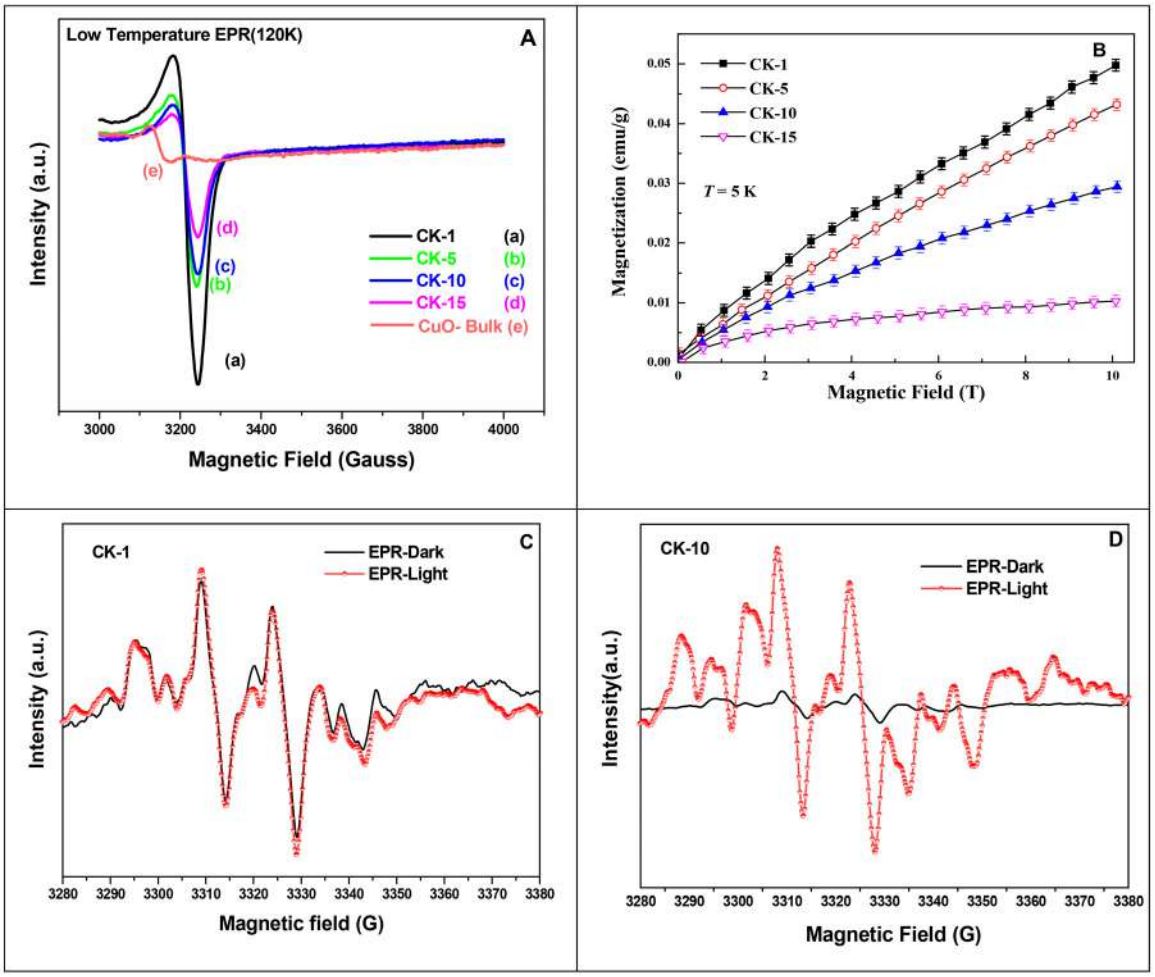

Fig. 8 (A) The EPR spectrum of CuO at 120 K for the different materials (a) CK-1; (b) CK-5; (c) CK-10; (d) CK-15 and (e) CuO bulk. (B) VSM magnetic data for the different CuO dispersed in KIT as (a) CK-1; (b) CK-5; (c) CK-10; and (d) CK-15; EPR data (3280 to 3380 G) for spin trapping of O_2^- radicals with DMPO in the presence and absence of light (C) CK-1; and (D) CK-10.

CuO as nanoclusters in the channels of KIT-6. KIT-6 (mainly diamagnetic mesoporous silica) does not affect the magnetic property, which is regulated by these two types of CuO present in KIT-6. At low temperature owing to the significant nano nature of the CuO nanoparticles as an effect of paramagnetic surface contribution arising from the presence of uncompensated Cu^{2+} ions at the surface of the particles as a function of particle size is more prevalent, as observed in Fig. 8B, where it is quite apparent that the magnetization increases as a function of decreasing particle size. As observed in the EPR signals the paramagnetic effect also increases with decreasing particle size due to the uncompensated Cu^{2+} spins at the surface of the nanoparticles where the particle size is small enough, so that the thermal energy can overcome the magnetic anisotropy energy, causing the magnetic moments to randomly flip direction, as discussed earlier, Fig. 8A. This paramagnetic part may also possess a strong component leading to strong magnetic effect for the CuO nanoparticles.

To further validate the involvement of superoxide as the active oxygen species, 5,5-dimethyl-1-pyrroline *N*-oxide (DMPO) was employed as a spin-trapping agent. As depicted in Fig. 8D, EPR spectra exhibited significant enhancement of distinct DMPO–$O_2^{\bullet-}$ adduct peaks[62–64] under light irradiation with the CK-10 photocatalyst, whereas the intensity of the DMPO–$O_2^{\bullet-}$ (Fig. 8D) adduct for the CK-1 sample is not that significant (Fig. 8C). However, there is a caution here; the CuO with Cu(II) is EPR active therefore the background for the CuO-DMPO is substantial. However, in the CK-10 sample there is a significant increase in the intensity of DMPO–$O_2^{\bullet-}$ thereby proving unequivocally the formation of superoxide radicals ($O_2^{\bullet-}$) in the presence of light irradiation, suggesting a sequential two-electron, two step reaction in the presence of light.

G. Photocatalytic activity

The photocatalytic activity of the different synthesized samples was assessed through the degradation of *ortho*-dichlorobenzene (*o*-DCB), a model organic pollutant, under visible light irradiation. The experimental details regarding the irradiation source have been provided earlier. Notably, all the catalysts having a band gap in the range of 2.86 to 2.44 eV lies in the

visible region. *Ex situ* ESI-MS spectroscopy was employed as a complementary technique to get a deeper understanding about the intermediates formed during the degradation process, thereby serving as a proof-of-concept for the reaction mechanism.

The Fig. 9A depicts the variation in photocatalytic activity of different samples. The detailed degradation data for the individual photocatalysts are presented in Fig. S1. It is crucial to note that the self-degradation of *o*-DCB in the absence of a photocatalyst is negligible (Fig. S2). Consequently, the percentage of degradation products is calculated using eqn (1).

The product percentage (PC %) is:

$$\mathrm{PC}\,(\%) = \frac{C_0 - C_i}{C_0} \times 100 \qquad (9)$$

where C_0 = UV-Vis intensity of *o*-DCB initially at 0 min; C_i = UV-Vis intensity of *o*-DCB without a particular photocatalyst at time t_i.

In order to provide a quantitative understanding, catalytic performance activity for the different photocatalysts in Fig. 9D shows the plot of *k vs.* particle size of CuO in KIT-6.

The $t_{1/2}$ (half-life) is defined as the time taken to degrade *o*-DCB to half its initial concentration, which is a measure of the efficiency of a photocatalyst. Conversely, the absence of *o*-DCB self-degradation during the experiment confirms its stability under visible irradiation from the lamp. The enhanced visible-light photocatalytic activity for *o*-DCB degradation is attributed to the modulation of the electronic band structure as a function of discretization of the electronic bands and potential of CuO nanoparticles inside the KIT-6 pore channels and the CuO nanoparticles dispersed over the surface of KIT-6 induced by varying % dispersion of CuO in KIT-6. Notably, CK-10 exhibited the highest activity (~74.5% degradation in 360 minutes, rate constant, $k = 37.94 \times 10^{-4}$ min^{-1}, $t_{1/2} = 182.65$ min). In comparison, the synthesized catalysts, CK-1, CK-5, and CK-15, displayed degradation efficiencies of 13.69% (360 min, $k = 4.09 \times 10^{-4}$ min^{-1}), 38% (360 min, $k = 13.28 \times 10^{-4}$ min^{-1}), and 53.64% (360 min, $k = 21.36 \times 10^{-4}$ min^{-1}, $t_{1/2} = 324.44$ min), respectively, as shown in Table 3. In the presence of the peroxide ion, the photocatalytic activity for the CK-10 photocatalyst is enhanced to around 80% degradation in 250 minutes thereby mainly increasing the kinetics of the process showing that the peroxide ions do play a strong role in the photocatalytic process. Triethanol ammine (TEA) [usually used as a h^+ quencher] shows a very strong effect over the reaction mechanism (Fig. 9B). The reaction rate is substantially slowed down to almost 8% degradation in 360 min

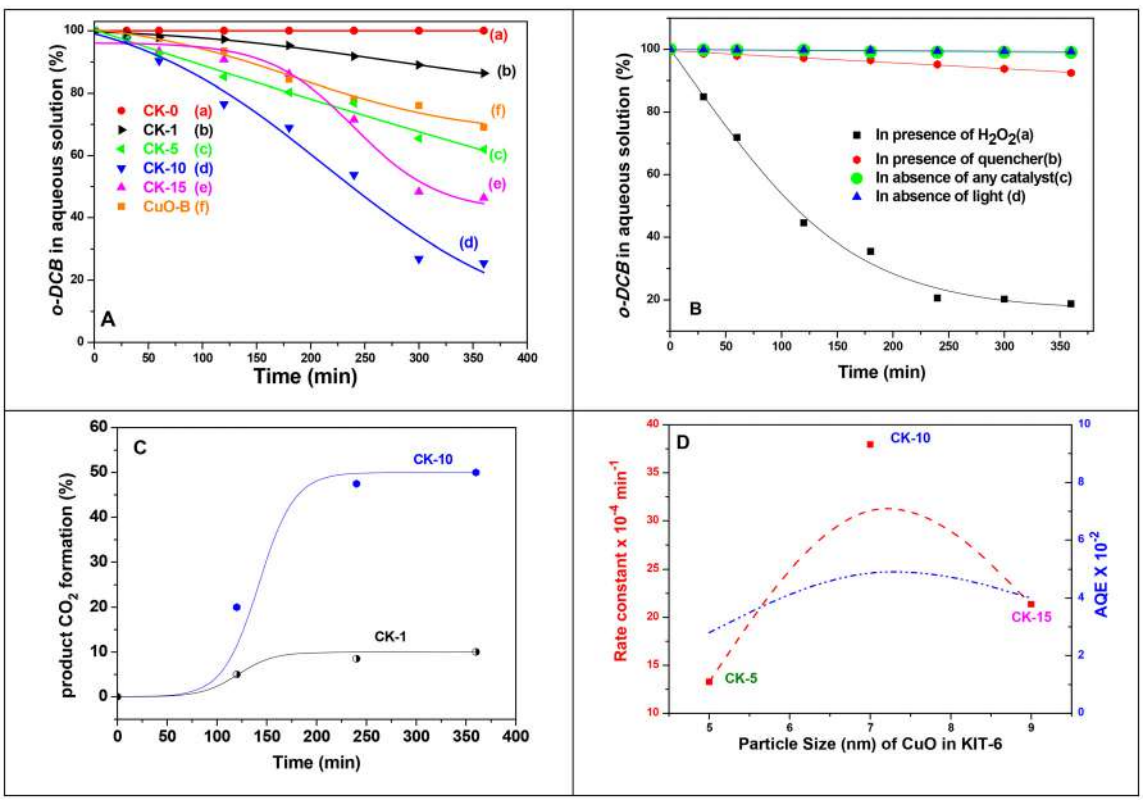

Fig. 9 (A) Degradation of *o*-DCB using (a) CK-0; (b) CK-1; (c) CK-5; (d) CK-10; (e) CK-15; and (f) CuO-bulk. (B) Control experiments for *o*-DCB degradation (a) in the presence of H_2O_2; (b) in the presence of a hole quencher; (c) self degradation of *o*-DCB; (d) in the absence of light; (C) CO_2 formation from *o*-DCB degradation for CK-1 and CK-10. (D) Variation of rate constant and apparent quantum yield with change in the particle size for CK-5, CK-10 and CK-15.

Table 3 Rate constant and $t_{1/2}$ values for the photocatalytic degradation of *o*-DCB by different CuO dispersed catalysts in KIT-6

Catalyst	% Degradation (in 360 minutes)	Rate constant (k) (min^{-1})	$t_{1/2}$ (min^{-1})
CK-0	0	—	—
CK-1	13.69%	4.09×10^{-4}	—
CK-5	38%	13.28×10^{-4}	—
CK-10	74.48%	37.94×10^{-4}	183
CK-15	53.64%	21.36×10^{-4}	324
CuO-bulk	30.91%	10.27×10^{-4}	—

showing the process to be a h^+ mediated process, however whether it is a direct hole mediated process or an indirect one is still an open question.

Two of the catalysts were checked for the complete mineralization in a closed quartz photocatalytic reactor (Fig. S8) with the parameters described in the SI (Fig. 9C).

The comparison between the different photocatalysts (Table 4) shows that the present photocatalyst is one of the best in the field, and therefore, a thorough mechanistic study through ESI-MS was conducted in order to discern the different intermediates formed in the solution.

H. *In situ* FT-IR study of the surface –OH groups and surface acidity and basicity

There are mainly two types of surface –OH groups present in KIT-6 and CuO dispersed KIT-6 photocatalysts. Bezrodna *et al.* reported at least two types of energy non-equivalent active centres which can be distinguished on the TiO_2 surface.[70,71] The first band at ~3411 cm^{-1} corresponds to the "weak" surface active sites, on which physisorbed water-like (H_2O) molecules are bound by hydrogen bonds with each other and with the OH– groups and the other band at ~3200 cm^{-1} is attributed to the water complexes or the chemisorbed water molecules, strongly bound with the TiO_2 surface like $H_2O\cdots HO–Ti$, {HOH···O(H)–Ti} over the TiO_2 surface.[72]However, for KIT-6 we also get two different surface –OH groups mainly at 3600 cm^{-1} and the other at 3200 cm^{-1} and in order to understand the physisorbed and chemisorbed species present we carried out *in situ* experiments as a function of temperature [Fig. 11F]. The IR-band at 3200 cm^{-1} decreases in intensity as a function of pressure and temperature from 50 to 150 °C. The percentage of physisorbed –OH [inset of Fig. 11G] as a function of temperature shows a definite decrease in the surface –OH groups for KIT-6 [Fig. 11G(b)]. However, once CuO is introduced, though there are two different physisorbed and chemisorbed groups, the lowering of the physisorbed percentage as a function of temperature shows a higher physisorbed:chemisorbed ratio. Thereby, this experiment indicates that the physisorbed surface –OH group for CuO-KIT-6 is a bit stronger as compared to that of KIT-6 only.

The acidity of the surface –OH groups of KIT-6 can be identified from the adsorption of a base like pyridine over the catalytic surface.[73,74] Chakraborty *et al.* reported different bands due to hydrogen bonded pyridine (1445 and 1596 cm^{-1}), strong Lewis bound pyridine (1623 and 1455 cm^{-1}), weak Lewis bound pyridine at 1575 cm^{-1}, pyridinium ion ring vibration due to pyridine bound to Brønsted acid sites (1546 and 1639 cm^{-1}) and a band which can be assigned to pyridine associated with both Brønsted and Lewis sites.[74] Upon the adsorption of the pyrindine, KIT-6 shows different peaks at 1639, 1596, 1492 and 1445 cm^{-1} (Fig. 10B). The adsorption bands at 1445 and 1596 cm^{-1}, shows the presence of hydrogen bonded pyridine; the band at 1492 cm^{-1} indicates the presence of both Brønsted and Lewis sites and the adsorption band at 1639 cm^{-1} indicates the Brønsted acid site. Upon dispersion of CuO in KIT-6 the adsorption of pyridine leads to different vibrational bands at 1596, 1546, 1495 and 1455 cm^{-1} (Fig. 10A). The bands at 1445 and 1596 cm^{-1} represent hydrogen bonded pyridine; the 1425 cm-1 band corresponds to Lewis bound pyridine and that at 1492 cm^{-1} correspond to both Brønsted and Lewis acid sites. Therefore, after dispersion of CuO in KIT-6 the major Brønsted acid sites are diminished to a large extent qualitatively.

Similarly, basic sites of the surface –OH groups can be qualitatively identified by the adsorption of acidic CO_2 over the catalytic surface, the formation of the HCO_3^- bands at 1273 cm^{-1} shows the presence of the surface basic –OH groups.[75] KIT-6 upon adsorption of the CO_2 forms the bicarbonate band with an intensity of 0.32 [Fig. 10D], whereas after dispersion of CuO in the KIT-6 medium the band at 1273 cm^{-1} has a typical intensity of 0.18 unit [Fig. 10C].

Therefore, qualitatively the surface basic sites also diminish for the CK catalysts as compared to KIT-6. The effect of lowering of the surface basic and Brønsted acidic sites upon dispersion of CuO will be further understood in the mechanistic part.

Table 4 A comparative evaluation of advanced catalytic systems for *o*-DCB

S. no.	Catalyst formulation (under visible light)	Conversion ratio (with time)	Ref.
1	V_2O_5 hollow spheres	45% (~7 h)	65
2	$AgInS_2/TiO_2$ composites	50% (~8 h)	66
3	Double shelled $ZnFe_2O_4$	74% (~7 h)	67
4	In_2S_3/In_2O_3 heterostructure	76.9% (~8 h)	68
5	In_2O_3@8%PANI composite	82.7% (~8 h)	69
6	10 wt% CuO in KIT-6	74.5% (~6 h)	Present work

I. Mechanistic understanding (MS study)

The ESI-MS study was performed to understand the different intermediates that are formed over the catalyst surface present in the solution form. ESI-MS study of different photocatalysts (Fig. 11) [CK-1 to CK-15] was performed to check the different intermediates formed over the course of the reaction in order to discern the mechanism for the degradation of *o*-DCB solution by the different photocatalysts.

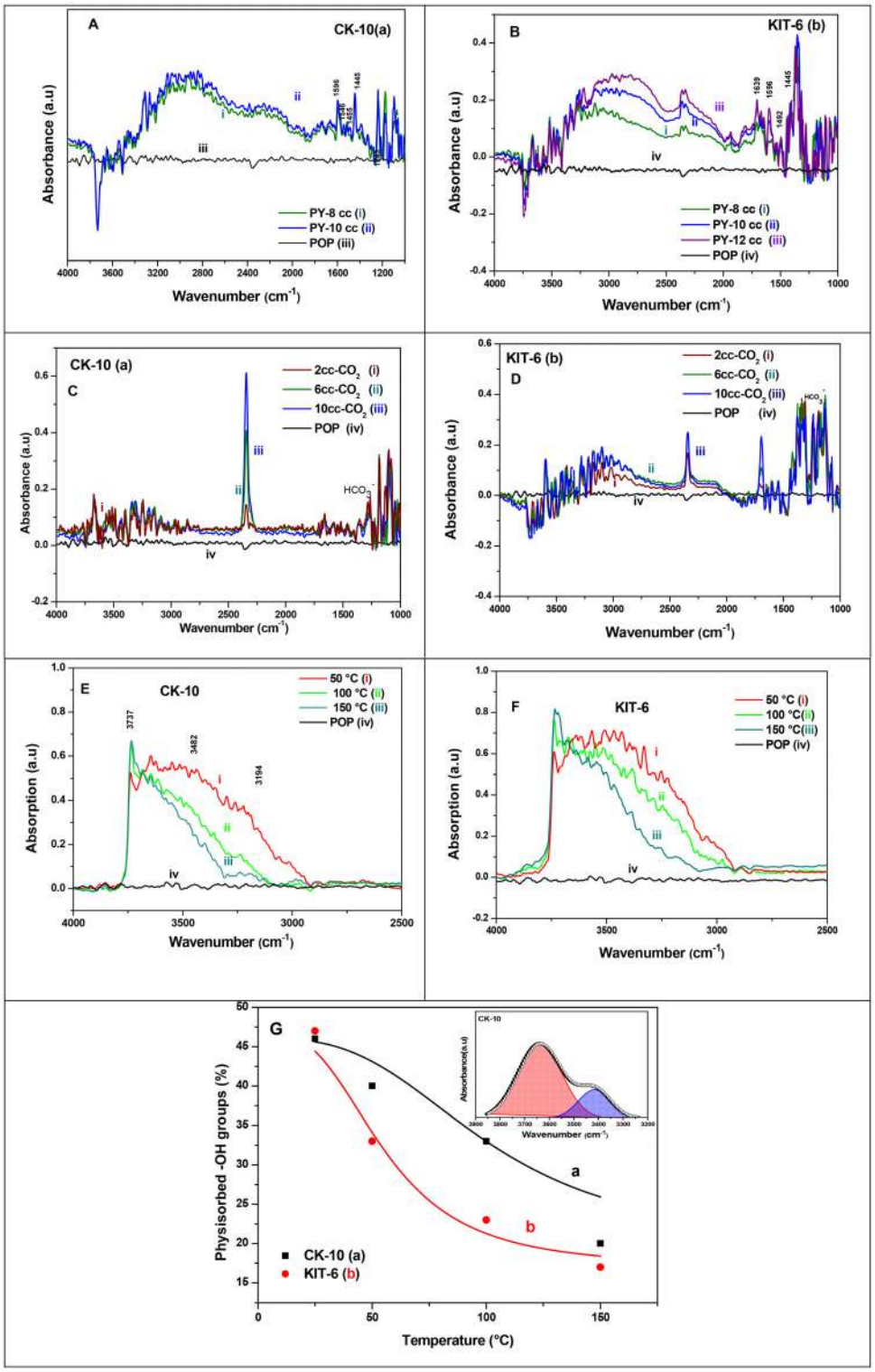

Fig. 10 (A) and (B) shows *in situ* FT-IR adsorption of pyridine samples showing the acidity of the surface −OH groups and (C) and (D) shows *in situ* FT-IR adsorption of CO_2 samples showing the basicity of the surface −OH groups over different samples of (a) KIT-6 and (b) CK-10. Deconvoluted FT-IR vibrational band in the stretching region (3900−3200 cm^{-1}) representing the stretching of the surface −OH groups-CK-10 (E) CK-10; (F) KIT-6 as a function of different temperature (a) 50 °C; (b) 100 °C; (c) 150 °C and (d) POP; (G) Alteration of physisorbed surface −OH (%) groups as a function of temperature. Inset contains the representative deconvoluted chemisorbed and physisorbed surface −OH groups for the CK-10 at 100 °C.

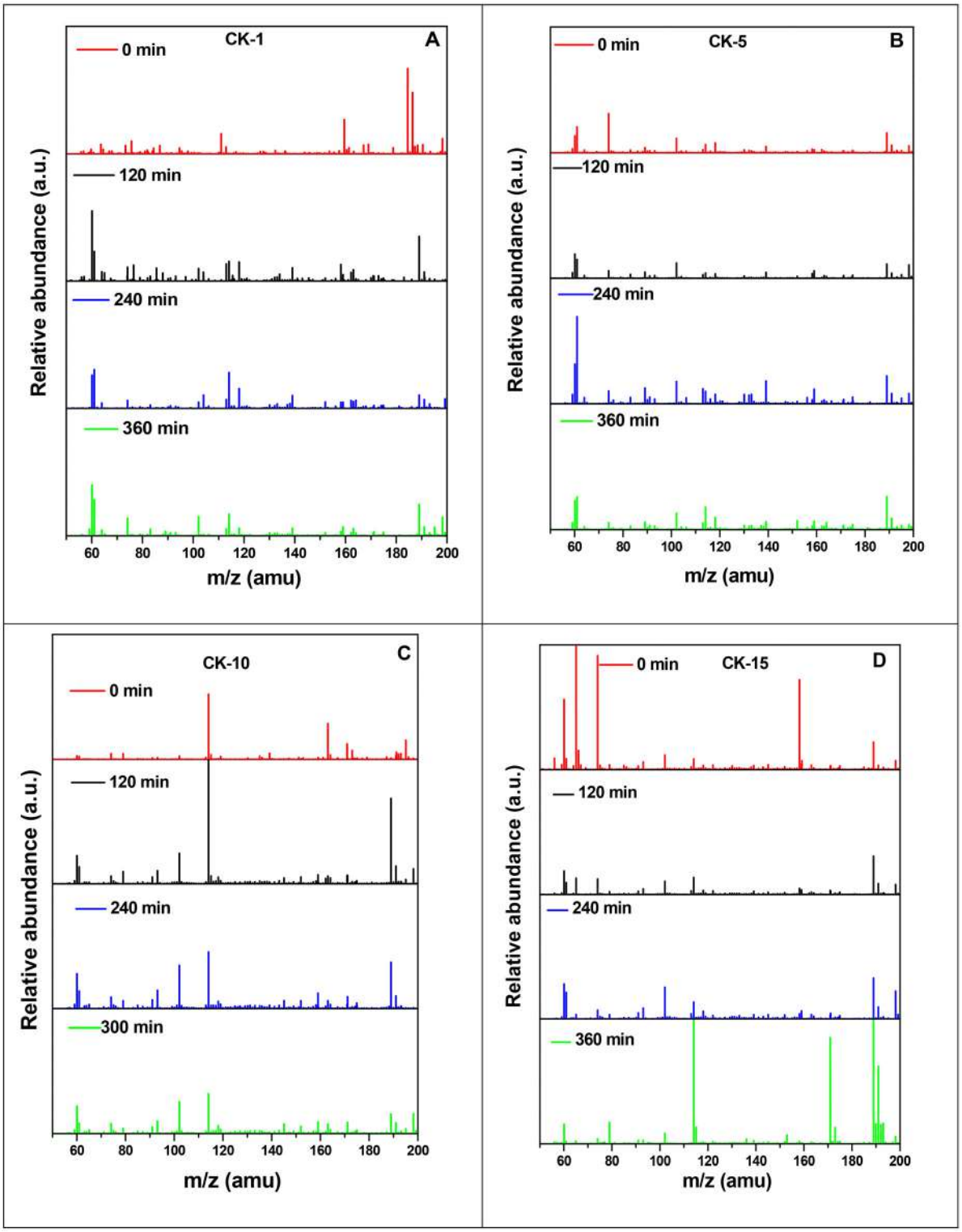

Fig. 11 *Ex situ* LC-MS data for the detection of intermediates as a function of catalytic degradation with time for the samples (A) CK-1; (B) CK-5; (C) CK-10; and (D) CK-15 at different time intervals of (a) 0 min; (b) 120 min; (c) 240 min and (d) 360 min. In the case of the CK-10 the intensities for the 120, 240, and 360 min are 1/10th that of the 0 min and are given for brevity.

1. CK-1. The CK-1 photocatalyst at time 0 min irradiation (Fig. 11A(a)) shows a prominent mass peak at *m*/*z* values of 163 and 113 and other lower intensity peaks at *m*/*z* 135, 96, 76, 63, and 88. The major peak at 163 represents *o*-DCB + H_2O and the other one at 113 represents catechol or enolate. This mainly shows that *o*-DCB has been adsorbed as enolates as

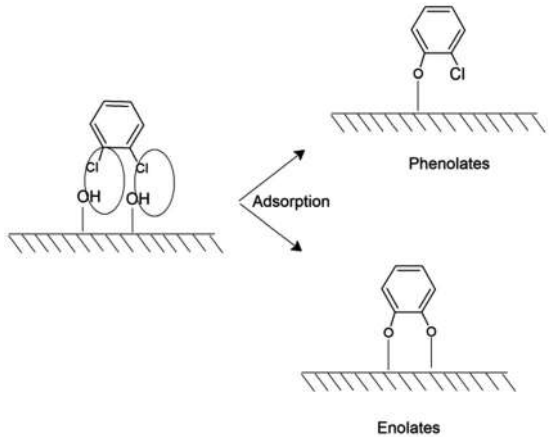

Scheme 3 Adsorption of *o*-DCB over the photocatalyst.

observed by Kumar *et al.*[31,32] over different catalytic surfaces. However, on solvation these enolates may also be found in the solution. The peak for the *o*-chlorophenol is also observed at ~135 (*m*/*z*) which is also observed for the CK-1 sample (Fig. 11A(a)) which shows that it is adsorbed as phenolate and is solvated as *o*-chlorophenol. This is presented in Scheme 3 for adsorption. The mass peak at *m*/*z* 96 represents phenol formed from the phenolate adsorbed species. The peak at 88 is ascribed to Cl_2 with H_2O which are formed as a result of the adsorption of the *o*-DCB as enolates or phenolates. The peak at 76 is mainly ascribed to benzene, formed as a fragmentation peak in the *o*-DCB solution. As the LC-MS starts from mass no. 50 onwards, the HCl peak is not observed but Cl_2 and H_2O peaks at *m*/*z* of 88 are observed. The adsorption of *o*-DCB will be more facilitated by the physisorbed -surface –OH groups as compared to that of the chemisorbed surface –OH groups. Upon the dispersion of the CuO over KIT-6, the overall physisorbed surface –OH groups increases (Fig. 10G), and the adsorption phenomena will be better with a higher CuO concentration over KIT-6.

Upon irradiation for 120 min (Fig. 11A(b)) different peaks are observed at *m*/*z* of 190, 158, 139, 120, 102, 85, 76, and 69. The mass peak at *m*/*z* 158 represents benzyl acetate.[76] It usually arises due to fragmentation products at *m*/*z* 77 and 43 and 108. The peak at 43 will not be observed here, however, mass peaks at 77 and 108 are observed. The strong peak at *m*/*z* 139 represents benzoic acetate as ester formed by benzoic acid and methanol. This also gives a fragmentation peak at 77 and 108. The next mass peak at *m*/*z* 120 mainly represents benzoic acid.[77] The next major peak at *m*/*z* 102 represents benzaldehyde. There are minor peaks observed at *m*/*z* 88. The peak at *m*/*z* 61 represents that of acetone. The mass peak at *m*/*z* 74 represents either benzene, butanol or an ester of CH_3-O-COO-C_2H_4 known as the McLafferty ion.[78] However, the ester has a minor fragmentation peak at 87 and 89 which are observed during the reaction confirming the mass peak at 74 can be ascribed to esters. Now the strongest peak at *m*/*z* 190 is mostly ascribed to a long chain aliphatic acid 3,4-dimethyl-2-hydroxy-3-oxo-pentandioic-acid formed by ring opening either by the McLafferty or a conjugation reaction.[79] The complete degradation mechanism is presented in Scheme 4.

2. CK-5. The different mass peaks for the CK-5 photocatalyst (Fig. 11B) are obtained at almost similar *m*/*z* values, as previously seen for CK-1. At 0 min, the different peaks present are at *m*/*z* values of 163, 113 amu and other lower intensity peaks at *m*/*z* values of 135, 96, 76, 63, and 88 amu. At different irradiation times like 120 min and 240 min, as discussed above, the major peaks are obtained at *m*/*z* 190, 158, 139, 120, 102, 85, 76, and 69 amu showing a similar reaction mechanism to that shown in Scheme 4 for this photocatalyst also.

3. CK-10. The degradation of *o*-DCB using the photocatalyst CK-10 (Fig. 11C) majorly shows peaks at *m*/*z* values of 163, 139, 114, 74, and 63 at 0 min of irradiation (Fig. 11C(a)). The peak at *m*/*z* 163 is attributed to *o*-DCB with H_2O, and those at *m*/*z* 114 and 139 represent enolates and phenolates, respectively, as discussed earlier. The peak at 74 mostly corresponds to doubly dechlorinated *o*-DCB and that at 63 represents the $Cl^{35.5}$ to $Cl^{37.5}$ isotopic ratios of 3 : 1. Therefore, for the CK-10 photocatalyst, the process of adsorption is similar to that of CK-1, as shown in Scheme 5. Effective higher irradiation time of 120 min for *o*-DCB degradation (Fig. 11C (b)) shows mass peaks at *m*/*z* 61, 74, 78, 102, 114, 159, 170, and 188. The peak at *m*/*z* 114 amu representing enolate, decreases considerably, and the peak at *m*/*z* 102 represents benzaldehyde; *m*/*z* 159 represents benzyl acetate as discussed for CK-1; *m*/*z* 188 represents 3,4-dimethyl-2-hydroxy-3-oxo-pentandioic-acid, formed by ring opening with McLafferty; *m*/*z* 61 represents acetone; *m*/*z* of 77 represents the McLafferty ion fragment. However, there is new peak at *m*/*z* 170 which mainly shows the loss of one –OH from *m*/*z* 188 representing mostly 3,4-dimethyl-3-oxo-pentandioic-acid, which is shown in Scheme 5. The EPR spin trapping experiment definitely shows the formation of the superoxide ion which mostly affects the formation of the different intermediates as shown in Scheme 5 and increases the kinetics of the oxidation reaction.[64,80,81]

4. CK-15. The intermediates formed by adsorption and photo-oxidation of *o*-DCB with photocatalyst CK-15 (Fig. 12D) shows different mass peaks at *m*/*z* values of 61, 74, and 158 at 0 min (Fig. 11D(a)). The major peak at an *m*/*z* value of 158 amu corresponds to the phenolate and H_2O together. However, the peaks at *m*/*z* values of 114 and 163 show very low intensities for the CK-15 photocatalysts at 0 min, indicating that the adsorbed species are phenolates and not enolates. The peak of *o*-DCB and H_2O is also missing here. The peaks at 74 and 61 as shown before are mostly ascribed to benzene and Cl moieties. After 120 min of irradiation, the mass peaks are obtained at *m*/*z* values of 61, 74, 93, 102, 114, 171, and 190 with the major peaks at the mass value at *m*/*z* 190, 114 and 60. The peak at *m*/*z* 190 corresponds mainly to a long chain aliphatic acid represented as 3,4-dimethyl-2-hydroxy-3-oxo-pentandioic-acid, as shown earlier, and the mass peak at *m*/*z* 170 corresponds to 3,4-dimethyl-3-oxo-pentandioic acid. However, interestingly there is a mass peak at *m*/*z* 114 representing enolates, showing the formation of enolates from phenolates. The mass

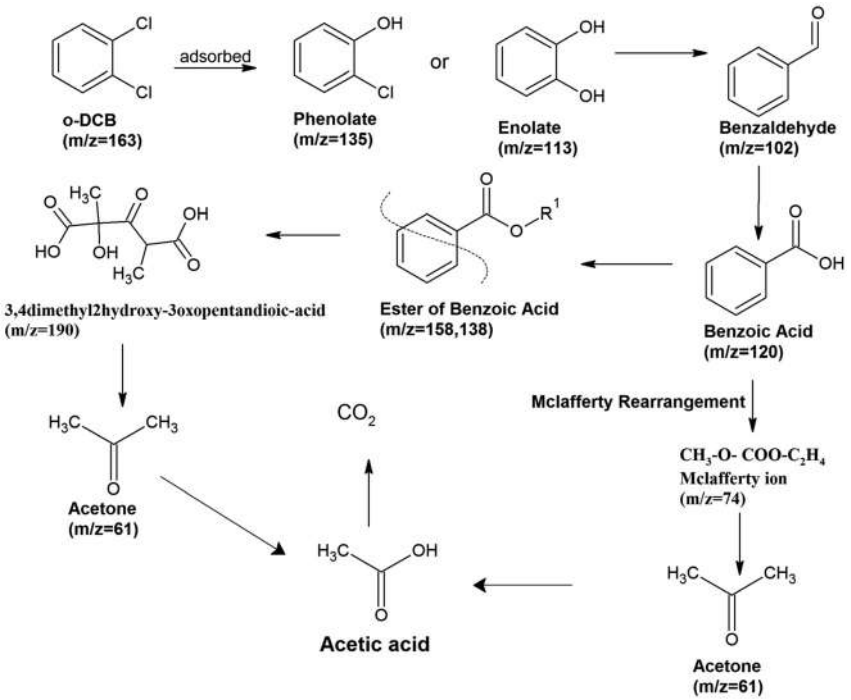

Scheme 4 Probable intermediates formed during photo-mineralization of *o*-DCB with the CK-1 catalyst.

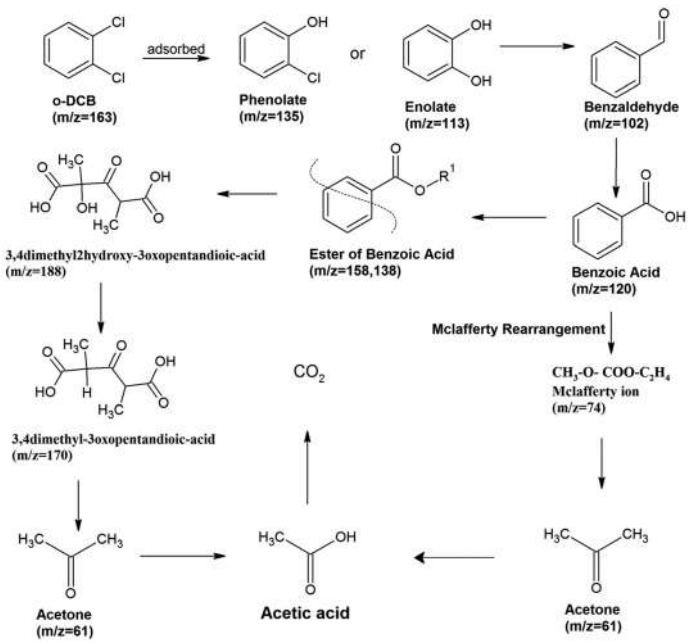

Scheme 5 Probable intermediates formed during photo-mineralization of *o*-DCB with the CK-10 catalyst.

peak at 102 *m*/*z* represents benzaldehyde and that at *m*/*z* 60 represents acetone. The other two mass peaks at *m*/*z* values of 74 and 93 represent the mass fragments formed for the McLafferty ions. After 240 min of irradiation, the different mass peaks only show a change in intensity. However, after 360 min of irradiation, the major mass peaks that are obtained are found at *m*/*z* values of 190 and 114 and a minor peak at 170, showing a major peak of adsorbed enolate along with the intermediate species of long chain aliphatic acid. CK-15 mainly follows Scheme 5. Mostly this describes the lowering of the photocatalytic activity for CK-15 as compared to that of CK-10 as the enolate product does not go downhill.

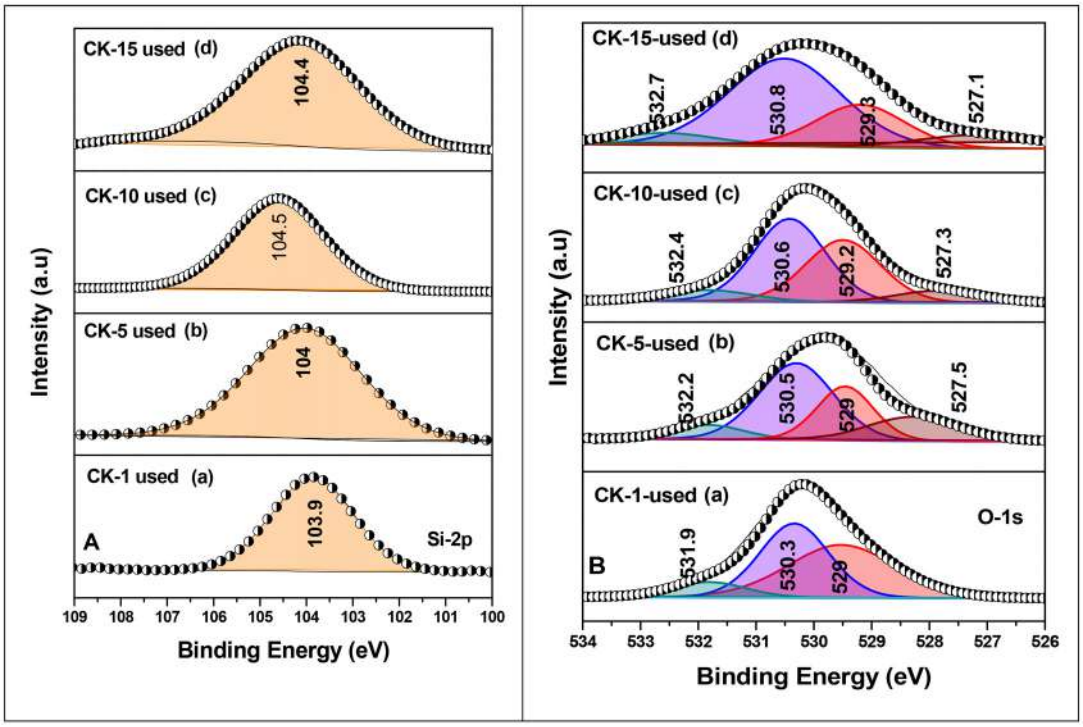

Fig. 12 Deconvoluted XPS spectra of (A) Si-2p and (B) O-1s for the used photocatalysts (a) CK-1; (b) CK-5; (c) CK-10; and (d) CK-15.

Another point worth mentioning is that the alteration in the magnetic property as a function of particle size is mainly attributed to the presence of uncompensated spins of Cu^{2+} at the surface, which may regulate some of the adsorption of the nucleophilic intermediates with definite spin orientation leading to either stronger/weaker formation of the particular intermediate over the catalytic surface. Therefore, it is quite possible that the uncompensated spin of paramagnetic Cu^{2+} may regulate certain intermediates.

J. XPS investigations of spent photocatalysts

XPS studies were conducted on the used photocatalysts to understand the effect of the surface oxidation of host/support KIT-6 and the different nanophotocatalysts of CuO dispersed within the channels of KIT-6 and present over the surface also. Post-catalytic activity XPS data show a slight increase in the binding energy of Si-2p (Fig. 12A) at 103.9 eV by around ~0.2 eV. However, CK-5 onwards there is an increase in the binding energy of Si-2p as a function of CuO dispersion. In the above schemes, different intermediates formed over the catalytic surface are shown, which are adsorbed as enolates, acetates, esters, and acids, both aliphatic and aromatic acids, mostly as O–Si–O as shown in Scheme 4. This draws electron density from Si as they will be attached to the Si of the SiO_2 (KIT-6) surface thereby Si will have a higher binding energy. Once we move from CK-1 to CK-15, stronger nucleophilic intermediates (Schemes 4 and 5) are formed, which will further increase the binding energy of Si, as observed in Si-XPS.

The O-1s XPS data post-catalysis show mainly three to four deconvoluted peaks at 529, 530.3 and 531 eV. As described earlier in the XPS section, the first peak represents the O attached with Cu, the second peak represents O attached with Si and the last one shows the surface hydroxyl groups. There is an alteration in the binding energy of O-1s representing the O attached to Cu as CK-1 (529 eV); CK-5 (529.5 eV); CK-10 (529.8 eV) and CK-15 (529.5 eV), respectively and that of O–Si in CK-1 (530.3 eV); CK-5 (530.8 eV); CK-10 (531 eV) and CK-15 (532 eV). These alterations are mostly due to the formation of different intermediates over O of CuO and O in SiO_2, as explained in Schemes 4 and 5. Therefore, it is quite clear that KIT-6 not only works as a support but also acts as the surface for the formation of different intermediates.

3. Discussion

These synthesised photocatalysts have CuO nanoparticles which are either dispersed in the mesoporous channels of KIT-6 or are dispersed over the surface of the KIT-6 host. The bulk CuO is a known p-type semiconductor,[7] which is observed similarly in the Mott–Schottky experiments. The XRD pattern and the STEM/HRTEM data show that CK-10 onwards, there are two types of CuO nanoparticles present in KIT-6: (a) those present as the nanocluster within the mesoporous channels of KIT-6 and (b) nanoparticles that are present mostly on the surface and are outside the mesoporous channels resulting in the XRD peaks (Fig. 1B) in the wide angle and those seen

STEM images (Fig. 3C and D). In CK-1, there are no CuO particles on the surface as they are completely present in the 3-D mesoporous channels of KIT-6. The particle size for these CuO nanoparticles systematically varies as a function of concentration in the host matrix and varies from 5 to 9 nm from CK-5 to CK-15. If extrapolated CK-1 will be having further small nanoparticles in the regime lower that 4 nm. Both the magnetic and the photocatalytic properties widely vary as a function of variance in the particle size of CuO in the mesoporous KIT-6 host. The surface magnetisation becomes stronger as the particle size reduces (Fig. 8B) and CK-1 shows the maximum surface magnetization. This is mostly due to the effect of the uncompensated spin present on the surface as is evidenced from the EPR properties of these materials (Fig. 8A), where CK-1 having the smallest particle size occupies the mesoporous channels and shows the maximum EPR signal. This is ascribed mainly to the lowering of the grain boundaries as a function of decreasing particle size, and CK-1 in the regime of 3–4 nm, shows very strong surface magnetisation, thereby enhancing the magnetic properties, as shown earlier in the literature by Chen *et al.* for around 13–17 nm particles.[57] KIT-6 or CK-0, being SiO_2, is diamagnetic and there is no electronic interaction between the CuO nanoclusters and KIT-6 (Fig. 7A), therefore, the manifestation of magnetic properties is mainly related to the domain of variation in the particle size of CuO. Rao *et al.*[18] opined the possibility of super-exchange phenomena in antiferromagnetic CuO between Cu^{2+} and O^{2-} and lower exchange for second nearest-neighbour Cu^{2+} ions leading to greater spin susceptibility in CuO.

The photocatalytic activity for the mineralization of *o*-DCB has an opposite trend with respect to the variation in the particle size. As the particle size increases, CK becomes a better photocatalyst up to CK-10, however, for CK-15, the photocatalytic activity diminishes. As a function of particle size, several properties of the photocatalyst changes: (a) the band gap alters (CK-1: 2.86 to CK-15: 2.59) mainly due to the quantum confinement effect of the nanoparticles; (b) surface area (665 to 480 $m^2\ g^{-1}$) and the pore size (5.56 to 5.3 Å) diminishes on moving from CK-1 to CK-15; (c) valence band potential also increases systematically as a function of particle size from CK-1 to CK-15 (Scheme 2: 4.71 to 4.92 eV); (d) surface charge variation: the surface becomes more negative as a function of CuO dispersion in KIT-6 (CK-1 to CK-15) at near neutral pH, which is majorly the pH of the reaction medium; (e) alteration in the different intermediates formed (Schemes 4 and 5) over the surface of CK-1 to CK-15; (f) alteration in the photocurrent and the difference in the carrier concentration of the semiconductor; and (g) the formation of the $O_2^{\bullet -}$ radicals in the presence of light for the CK-10 photocatalysts (Fig. 9D). The degradation of *o*-DCB is a reaction that takes place in the liquid medium and the effect of the surface area becomes negligible; however, the pore size may definitely play a role in allowing the analyte to access the photocatalyst. The alteration in the band gap as a function of particle size signifies an increase in the energy of h^+/e^- and lowering of the back electron transfer dynamics. However, as the catalytic activity of CK-15, having a higher band gap, is lower than that of CK-10, this cannot be the primary reason affecting the photocatalytic activity. Degradation of *o*-DCB is an oxidation reaction, and the increase in the valence band potential definitely will play a significant role, as it increases as a function of particle size. However, for CK-15 the surface charge is highly negative as compared to that of CK-10. The intermediates that are formed over the photocatalytic surface are mainly strong nucleophiles and will be less stable over the more negative surface making CK-15 an inferior catalyst as compared to that of CK-10. These reactions majorly involve nucleophilic intermediates and are therefore more affected by the surface acidic sites than the surface basic sites, and upon CuO dispersion, the Lewis and hydrogenated surface acidic sites increase, whereas the surface basic sites decrease. Therefore, the different nucleophilic intermediates are more stabilised, leading to better photocatalytic activity of CK. Also in CK-15 the bulk property is quite significant, which can be readily evidenced from the XRD and STEM results. The bulk CuO and CK-1 to CK-5 are mostly p-type semiconductors. However, CK-10 and CK-15 are p–n type heterojunction and not just a p-type semiconductor. This is probably due to the effect of the particles present within the pore and certain particles present over the surface leading to the formation of a heterojunction. However, for CK-15, as the bulk feature is more prominent, the photocurrent reduces considerably compared to that in CK-10. This has a detrimental effect on the photocatalytic effect of the CK-15 catalyst. A close look over the different intermediates formed over the catalytic surface also gives a strong clue. The enolates which are formed as an adsorbate product get strongly stabilised over CK-15 and do not reduce leading to poor photocatalytic activity for CK-15. CK-10 has a very strong valence band potential, higher band gap, highest photocurrent, and optimum surface charge resulting in facile adsorption and desorption of intermediates, making it the best photocatalyst in the series. Also the Schottky barrier mostly formed by the p-n heterojunction in the CK-10 photocatalyst is an added advantage. Finally, the magnetic properties and the photocatalytic properties are both affected by the variation in the particle size of the CuO nanoparticles in the pore channels of KIT-6, although the two effects have an opposite trend as a function of particle size. The alteration in the magnetic properties as a function of the particle size is more or less regulated by the uncompensated Cu^{2+} spin present over the surface of the CuO nanoparticles. This may in a certain way stabilize/destabilize certain nucleophilic intermediates with a particular spin orientation in its structure, thereby to a certain extent may regulate the kinetics of the catalytic reactions. However, the role of magnetism in influencing the photocatalytic effect remains an open question for this manuscript and requires further research. One fact which is very pertinent and is worth mentioning here is that KIT-6 is not only a support or a host, but also definitely takes part in the photocatalytic reaction. The post catalytic XPS data show that the intermediates are formed definitely over the Si sites along with the Cu sites. This is only possible if the surface –OH groups of KIT-6 act synergistically with those of

CuO. KIT-6 helps in the formation of CuO nanoclusters and the intermediates are formed over KIT-6 and CuO. Thereby as the concentration of CuO increases, the surface CuO nanoparticles and the CuO nanoparticles present in the mesoporous channels and SiO_2 play a substantial role. Therefore, the intermediates with the phenolic or the catecholic ring moiety will possess more ring strain over larger particle size materials, making them a better photocatalyst for the degradation of *o*-DCB which is inherently a tougher molecule to mineralize by photocatalysis. All the photocatalysts mineralize *o*-DCB (Fig. 9C) and the experiments conducted (Fig. S9) show the oxidation of *o*-DCB by these catalysts to CO_2. The AQE also improves as a function of particle size for these photocatalysts (Fig. 9D). The challenge for developing a suitable catalyst for pollutant degradation lies in finding the optimum dispersion of the catalyst in the host to find a balance between maximizing the pore filling while minimizing the presence of the catalyst particle on the surface of the host, so as to get the highest number of effective catalytic sites.

4. Conclusions

CuO in the nanoregime was synthesised by a facile wet impregnation technique where the particles of almost lower than 5 nm were obtained as a function of dispersion in the synthesized KIT-6 mesoporous host moieties. The XRD and STEM show the presence of the CuO nanoparticles in the 3-D mesoporous channels of KIT-6 in CK-1 to CK-5 and the presence of CuO in the mesoporous channels and on the surface for CK-10 and CK-15. The STEM shows that the particle size increases as more CuO is loaded in the host moiety and the EELS along with the elemental mapping shows that the particles present in the cubic mesoporous structures of KIT-6 are phase pure CuO. The EPR experiments effectively illustrate the effect of weak paramagnetic behaviour as a function of particle size mostly due to uncompensated Cu^{2+} spins present over the surface of the nanoparticles, which is also reflected in the magnetic properties of these nanomaterials. All these nanomaterials possess surface magnetism at 5 K as compared to the CuO bulk which may or may not have an implication on their catalytic properties. CK-10 showed the highest catalytic activity showing a 74.5% degradation over a period of 6 hours owing to a number of favourable factors like (a) the highest photocurrent response; (b) high positive VB potential showing high oxidative ability; (c) reduced recombination due to high band gap and (d) optimum surface charge that favours adsorption and desorption of the intermediates. The magnetic and photocatalytic properties show an opposite trend with increasing particle size, even though CK-15 is an inferior photocatalyst owing to its bulk-like nature. The mechanistic understanding for the degradation of *o*-DCB over these photocatalysts has been discerned. *o*-DCB is mainly adsorbed as phenolates or enolates over CK-1 to CK-5 and the different intermediates formed are benzaldehyde, benzoic acid, ester of benzoic acid, long chain aliphatic acid, acetone, acetic acid and finally CO_2. For CK-10 and CK-15, the only difference is the presence of another long chain aliphatic acid, owing to the enhanced number of surface acidic sites. However, in CK-15 the high negative surface charge mostly leads to a poorer adsorption of the enolates over the catalytic surface making it an inferior photocatalyst compared to CK-10.

Author contributions

S. M. synthesized the catalysts and performed all the photocatalytic experiments and all other characterization experiments, processing the data and helped in the writing of the manuscript. A. K. has helped in the carrying out the photocatalytic reaction in a closed photocatalytic reactor and recording the data set in EGA. D. T. has helped in recording XPS data; S. H. R. has helped in recording the ESI-MS data; D. S. has taken and understood and processed SAXS data; A. S. and A. R. has contributed by recording the HR-TEM/STEM and EELS mapping data; M. D. M. has recorded the magnetic VSM data. K. B. has conceptualised the project, written and corrected the manuscript and has guided in all grounds. A. K. T. was involved in conceptualization of the project and checked the manuscript, corrected the manuscript and has given invaluable scientific input throughout the course of this work and manuscript writing. He has guided S. M., A. K. all through.

Conflicts of interest

The authors report no conflict of interest.

Data availability

Data will be available on demand from the authors. Supplementary information (SI): Fig. S1: UV Visible plots for the degradation of *o*-DCB using (a) CK-0; (b) CK-1; (c) CK-5; (d) CK-10; (e) CK-15; and (f) bulk-CuO. Fig. S2: UV visible plots for the control experiments (a) *o*-DCB self-degradation, (b) degradation in the absence of light and (c) degradation in the presence of a quencher. Fig. S3: Kubelka Munk plot for the band gap of CK-0 (KIT-6). Fig. S4: Deconvoluted XPS data for Cu-2p for different samples: (a) CK-1; (b) CK-5; (c) CK-10; and (d) CK-15. Fig. S5: Pore size distribution of (a) CK-1; (b) CK-5; (c) CK-10; and (d) CK-15. Fig. S6: Deconvoluted XPS data for Cu-2p for the different photocatalytic samples used after *o*-DCB degradation: (a) CK-1; (b) CK-5; (c) CK-10; and (d) CK-15. Fig. S7A: HRTEM image of CK-0 *i.e.* pristine synthesised KIT-6 showing mesoporous channels. Fig. S7B: HRTEM image of CK10 along with its elemental mapping. Fig. S8: The experiments have been conducted in the above photocatalytic reactor. Fig. S9: Mass spectra for the products formed by (1) CK-1 and (2) CK-10 in the closed photocatalytic reactor along with (3) the mass of air before any reaction showing the amount of CO_2 produced as a function of time using different

photocatalysts. Fig. S10: X-ray diffraction data from (θ = 10° to 70°) for (A) CK-10 and (B) CK-10 post activity Fig. S11: DR-IR-FT-IR spectra for pyridine from the pyridine–air mixture formed in the glass bulb Table S1: Calculated apparent quantum efficiencies of different photocatalysts. Table S2: Optimisation parameters for the calculation of the bandgap using the hybrid potential of HSE-06. See DOI: https://doi.org/10.1039/d5nr03258j.

Acknowledgements

A. K. T. and S. M. sincerely acknowledge SERB for the J. C. Bose Fellowship (Grant Number: JCB/2023/000008 from ANRF, DST). S. M. acknowledges Shri. Debdulal Bag for carrying out N_2-adsorption measurements; Shri. Dnyaneshwar Avhad of TIFR for the conduction of the EPR measurements and Shri Prakash Mandal for helping out with the KIT-6 synthesis. A. S. and A. R. acknowledges beamtime in the SATHI HRTEM facility at IIT Kharagpur, and the funding from BRNS for availing the beamtime.

References

1 C. Burda, X. Chen, R. Narayanan and M. A. El-Sayed, *Chem. Rev.*, 2005, **105**, 1025–1102.
2 P. Wang, H. Liao, Y. Chen, X. Tao, Y. Gan, H. Deng, Y. Fu, Y. Tang, L. Wu and L. Tan, *ACS Catal.*, 2024, **14**, 8116–8129.
3 K. Bhattacharyya, S. Varma, D. Kumar, A. K. Tripathi and N. M. Gupta, *J. Nanosci. Nanotechnol.*, 2005, **5**, 797–805.
4 L. Wu, H. Lian, J. J. Willis, E. D. Goodman, I. S. McKay, J. Qin, C. J. Tassone and M. Cargnello, *Chem. Mater.*, 2018, **30**, 1127–1135.
5 Y. K. Jeong and G. M. Choi, *J. Phys. Chem. Solids*, 1996, **57**, 81–84.
6 D. Wu, Q. Zhang and M. Tao, *Phys. Rev. B: Condens. Matter Mater. Phys.*, 2006, **73**, 235206.
7 F. P. Koffyberg and F. A. Benko, *J. Appl. Phys.*, 1982, **53**, 1173–1177.
8 F. Marabelli and G. B. Parravicini, *Phys. B*, 1994, **199**, 255–256.
9 G. Papadimitropoulos, N. Vourdas, V. E. Vamvakas and D. Davazoglou, *Thin Solid Films*, 2006, **515**, 2428–2432.
10 S. Rehman, A. Mumtaz and S. K. Hasanain, *J. Nanopart. Res.*, 2011, **13**, 2497–2507.
11 Y. S. Chaudhary, A. Agrawal, R. Shrivastav, V. R. Satsangi and S. Dass, *Int. J. Hydrogen Energy*, 2004, **29**, 131–134.
12 A. Chowdhuri, V. Gupta, K. Sreenivas, R. Kumar, S. Mozumdar and P. K. Patanjali, *Appl. Phys. Lett.*, 2004, **84**, 1180–1182.
13 X. P. Gao, J. L. Bao, G. L. Pan, H. Y. Zhu, P. X. Huang, F. Wu and D. Y. Song, *J. Phys. Chem. B*, 2004, **108**, 5547–5551.
14 J. Chen, S. Z. Deng, N. S. Xu, W. Zhang, X. Wen and S. Yang, *Appl. Phys. Lett.*, 2003, **83**, 746–748.
15 J. A. Switzer, H. M. Kothari, P. Poizot, S. Nakanishi and E. W. Bohannan, *Nature*, 2003, **425**, 490–493.
16 S. E. Bogenrieder, J. Beßner, A. K. Engstfeld and T. Jacob, *J. Phys. Chem. C*, 2024, **128**, 9693–9704.
17 H. J. Koo and M. H. Whangbo, *Inorg. Chem.*, 2003, **42**, 1187–1192.
18 T. Shimizu, T. Matsumoto, A. Goto, T. V. C. Rao, K. Yoshimura and K. Kosuge, *Phys. Rev. B: Condens. Matter Mater. Phys.*, 2003, **68**, 224433.
19 N. Tang, J. Wen, Y. Zhang, F. Liu, K. Lin and Y. Du, *ACS Nano*, 2010, **4**, 241–250.
20 V. Dupuis, G. Khadra, J. M. Montejano-Carrizales, F. Tournus, F. Aguilera-Granja and A. Tamion, *ACS Appl. Nano Mater.*, 2019, **2**, 2864–2872.
21 S. Bai, X. Shen, G. Zhu, M. Li, H. Xi and K. Chen, *ACS Appl. Mater. Interfaces*, 2012, **4**, 2378–2386.
22 M. Diekmann, G. Koch, M. König and T. Ressler, *ChemCatChem*, 2018, **10**, 5459–5467.
23 C. Adamo, V. Dillet and V. Barone, *Chem. Phys. Lett.*, 1996, **263**, 113–118.
24 K. Nishida, T. Tojo, T. Kondo and M. Yuasa, *Sci. Rep.*, 2021, **11**, 2046.
25 J. Fan, C. Yu, J. Lei, Q. Zhang, T. Li, B. Tu, W. Zhou and D. Zhao, *J. Am. Chem. Soc.*, 2005, **127**, 10794–10795.
26 D. Zhao, J. Sun, Q. Li and G. D. Stucky, *Chem. Mater.*, 2000, **12**, 275–279.
27 X. Wang, Y. Zhang, W. Luo, A. A. Elzatahry, X. Cheng, A. Alghamdi, A. M. Abdullah, Y. Deng and D. Zhao, *Chem. Mater.*, 2016, **28**, 2356–2362.
28 S. Sareen, V. Mutreja, S. Singh and B. Pal, *J. Colloid Interface Sci.*, 2016, **461**, 203–210.
29 M. Khanmohammadi, J. R. Shahrouzi and F. Rahmani, *Environ. Sci. Pollut. Res.*, 2021, **28**, 862–879.
30 P. Dai, L. Zhang, G. Zhang, G. Li, Z. Sun, X. Liu and M. Wu, *Mater. Res. Bull.*, 2014, **56**, 119–124.
31 A. Kumar, D. Tyagi, S. Varma, H. Chand, V. Krishnan, K. Bhattacharyya and A. K. Tyagi, *Mater. Adv.*, 2024, **5**, 1301–1331.
32 K. Bhattacharyya, A. Kumar, D. Tyagi, A. K. Tripathi and A. K. Tyagi, *ChemPhysChem*, 2024, **25**, e202300472.
33 A. Kumar, D. Tyagi, R. Kumar, M. Ghosh, B. P. Mandal, A. Roy, S. Nath, A. K. Tyagi and K. Bhattacharyya, *J. Mater. Chem. A*, 2025, **13**, 19795.
34 M. Roso, C. Boaretti, R. Bonora, M. Modesti and A. Lorenzetti, *Ind. Eng. Chem. Res.*, 2018, **57**, 16635–16644.
35 Z. Shayegan, F. Haghighat and C.-S. Lee, *Chem. Eng. J.*, 2019, **357**, 533–546.
36 G. Kresse and D. Joubert, *Phys. Rev. B: Condens. Matter Mater. Phys.*, 1999, **59**, 1758.
37 P. E. Blöchl, *Phys. Rev. B: Condens. Matter Mater. Phys.*, 1994, **50**, 17953.
38 J. P. Perdew, J. A. Chevary, S. H. Vosko, K. A. Jackson, M. R. Pederson, D. J. Singh and C. Fiolhais, *Phys. Rev. B: Condens. Matter Mater. Phys.*, 1992, **46**, 6671.
39 K. Bhattacharya, A. K. Tripathi, G. K. Dey and N. M. Gupta, *J. Nanosci. Nanotechnol.*, 2005, **5**, 790–796.

40 H. J. Monkhorst and J. D. Pack, *Phys. Rev. B*, 1976, **13**, 5188.
41 S. L. Dudarev, G. A. Botton, S. Y. Savrasov, C. J. Humphreys and A. P. Sutton, *Phys. Rev. B: Condens. Matter Mater. Phys.*, 1998, **57**, 1505.
42 H. J. S. Ge and M. Ernzerhof, *J. Chem. Phys.*, 2006, **124**, 219906–219901.
43 T.-W. Kim, F. Kleitz, B. Paul and R. Ryoo, *J. Am. Chem. Soc.*, 2005, **127**, 7601–7610.
44 A. Vinu, N. Gokulakrishnan, V. V. Balasubramanian, S. Alam, M. P. Kapoor, K. Ariga and T. Mori, *Chem. – Eur. J.*, 2008, **14**, 11529–11538.
45 A. Duan, T. Li, Z. Zhao, B. Liu, X. Zhou, G. Jiang, J. Liu, Y. Wei and H. Pan, *Appl. Catal., B*, 2015, **165**, 763–773.
46 P. Mandal, A. Kumar, J. Bahadur, M. D. Mukadam, D. Sen and K. Bhattacharyya, *ACS Appl. Nano Mater.*, 2024, **7**, 17533–17552.
47 I. Breßler, J. Kohlbrecher and A. F. Thünemann, *Appl. Crystallogr.*, 2015, **48**, 1587–1598.
48 D. Tyagi, K. Scholz, S. Varma, K. Bhattacharya, S. Mali, P. S. Patil and S. R. Bharadwaj, *Int. J. Hydrogen Energy*, 2012, **37**, 3602–3611.
49 P. Kubelka, *Z. Tech. Phys.*, 1931, **12**, 593–601.
50 S. A. Tolba, K. M. Gameel, B. A. Ali, H. A. Almossalami and N. K. Allam, in *Density Functional Calculations-Recent Progresses of Theory and Application*, IntechOpen, 2018.
51 M. M. Abrar, A. Kabir and S. S. Nishat, *Mater. Today Commun.*, 2022, **32**, 103923.
52 K. Bhattacharyya, G. P. Mane, V. Rane, A. K. Tripathi and A. K. Tyagi, *J. Phys. Chem. C*, 2021, **125**, 1793–1810.
53 C. N. R. Rao, G. U. Kulkarni, P. J. Thomas and P. P. Edwards, *Chem. – Eur. J.*, 2002, **8**, 28–35.
54 K. Tabata, Y. Hirano and E. Suzuki, *Appl. Catal., A*, 1998, **170**, 245–254.
55 N. Wang, X. Li, X. Lian, Q. Zhuang, J. Wang, J. Li, H. Qian, K. Miao, Y. Wang, X. Luo and G. Feng, *Inorg. Chem.*, 2024, **63**, 4393–4403.
56 N. S. Rao, S. Bale, M. Purnima, C. Srinivasu, M. A. Samee, K. S. Kumar and S. Rahman, *Phys. B*, 2009, **404**, 1785–1789.
57 G. N. Rao, Y. D. Yao and J. W. Chen, *IEEE Trans. Magn.*, 2005, **41**, 3409–3411.
58 T. D. Clemons, R. H. Kerr and A. Joos, in *Comprehensive nanoscience and nanotechnology: Biological nanoscience*, Elsevier, 2019, vol. 3, pp. 193–210.
59 S. Åsbrink and L. J. Norrby, *Struct. Sci.*, 1970, **26**, 8–15.
60 A. Punnoose, H. Magnone, M. S. Seehra and J. Bonevich, *Phys. Rev. B: Condens. Matter Mater. Phys.*, 2001, **64**, 174420.
61 A. S. A. Raj, G. Madhu and V. Biju, *J. Solid State Chem.*, 2019, **278**, 120911.
62 K. Thawrani, K. Bhattacharya, D. Khushalani and J. Dasgupta, *J. Mater. Chem. A*, 2025, **13**, 28934–28943.
63 A. Kumar, D. Tyagi, S. Mitra, J. Bahadur, A. K. Tyagi and K. Bhattacharyya, *Mater. Adv.*, 2025, DOI: 10.1039/D5MA00954E.
64 S. He, Z. Hu, C. He, S. Tian, G. Ouyang, Z. Lin and J. Fang, *Angew. Chem.*, 2025, **137**, e202424827.
65 B. Liu, X. Li, Q. Zhao, J. Liu, S. Liu, S. Wang and M. Tadé, *J. Mater. Chem. A*, 2015, **3**, 15163–15170.
66 B. Liu, X. Li, Q. Zhao, J. Ke, M. Tadé and S. Liu, *Appl. Catal., B*, 2016, **185**, 1–10.
67 B. Liu, X. Li, Q. Zhao, Y. Hou and G. Chen, *J. Mater. Chem. A*, 2017, **5**, 8909–8915.
68 F. Zhang, X. Li, Q. Zhao and A. Chen, *J. Phys. Chem. C*, 2016, **120**, 19113–19123.
69 F. Zhang, X. Li, Q. Zhao, G. Chen and Q. Zhang, *Appl. Catal., B*, 2020, **263**, 118278.
70 T. Bezrodna, G. Puchkovska, V. Shymanovska, J. Baran and H. Ratajczak, *J. Mol. Struct.*, 2004, **700**, 175–181.
71 T. Bezrodna, G. Puchkovska, V. Shimanovska, I. Chashechnikova, T. Khalyavka and J. Baran, *Appl. Surf. Sci.*, 2003, **214**, 222–231.
72 K. Bhattacharyya, S. Varma, A. K. Tripathi, S. R. Bharadwaj and A. K. Tyagi, *J. Phys. Chem. B*, 2009, **113**, 5917–5928.
73 Q. Pan, A. Ramanathan, W. K. Snavely, R. V. Chaudhari and B. Subramaniam, *Ind. Eng. Chem. Res.*, 2013, **52**, 15481–15487.
74 B. Chakraborty and B. Viswanathan, *Catal. Today*, 1999, **49**, 253–260.
75 J. C. Lavalley, *Catal. Today*, 1996, **27**, 377–401.
76 T. Clark, T. M. Knox, M. A. McKervey, H. Mackle and J. J. Rooney, *J. Am. Chem. Soc.*, 1979, **101**, 2404–2410.
77 T. M. Nickels, A. L. Ingram, D. K. Maraoulaite and R. L. White, *Thermochim. Acta*, 2015, **614**, 157–162.
78 M. Takayama, M. Hashimoto, K. Ohshimo, F. Misaizu, M. Ubukata and K. Nagatomo, *Phys. Chem. Chem. Phys.*, 2025, **27**, 261–269.
79 M. Huang, Y. Lin, X. Huang, X. Liu, X. Guo, C. Hu, W. Zhao, X. Gu, L. Fang and W. Zhang, *Atmos. Pollut. Res.*, 2015, **6**, 209–219.
80 B. Dai, J. Guo, C. Gao, H. Yin, Y. Xie and Z. Lin, *Adv. Mater.*, 2023, **35**, 2210914.
81 S. Wang, Y. Li, X. Wang, G. Zi, C. Zhou, B. Liu, G. Liu, L. Wang and W. Huang, *J. Mater. Sci. Technol.*, 2022, **104**, 155–162.